ACS APPLIED MATERIALS & INTERFACES

Research Article

Cite This: ACS Appl. Mater. Interfaces 2018, 10, 29608−29621

www.acsami.org

Understanding the Role of Minor Molybdenum Doping in $LiNi_{0.5}Co_{0.2}Mn_{0.3}O_2$ Electrodes: from Structural and Surface Analyses and Theoretical Modeling to Practical Electrochemical Cells

Ortal Breuer,[†] Arup Chakraborty,[†] Jing Liu,[‡] Tatyana Kravchuk,[§] Larisa Burstein,[⊥] Judith Grinblat,[†] Yaron Kauffman,[∥] Alexandr Gladkih,[⊥] Prasant Nayak,[†] Merav Tsubery,[†] Anatoly I. Frenkel,[#] Michael Talianker,[▽] Dan T. Major,[†] Boris Markovsky,[†] and Doron Aurbach*[,†]

[†]Department of Chemistry, Bar-Ilan University, Ramat Gan 52900, Israel

[‡]Department of Physics, Manhattan College, Riverdale, New York 10471, United States

[§]Solid State Institute and [∥]Department of Materials Science and Engineering, Technion—Israel Institute of Technology, Haifa 32000, Israel

[⊥]The Wolfson Applied Materials Research Centre, Tel-Aviv University, Tel-Aviv 69978, Israel

[#]Department of Materials Science and Chemical Engineering, Stony Brook University, Stony Brook, New York 11794, United States

[▽]Department of Materials Engineering, Ben-Gurion University of the Negev, Beer-Sheva 84105, Israel

Supporting Information

ABSTRACT: Doping $LiNi_{0.5}Co_{0.2}Mn_{0.3}O_2$ (NCM523) cathode material by small amount of Mo^{6+} ions, around 1 mol %, affects pronouncedly its structure, surface properties, and electronic and electrochemical behavior. Cathodes comprising Mo^{6+}-doped NCM523 exhibited in Li cells higher specific capacities, higher rate capabilities, lower capacity fading, and lower charge-transfer resistance that relates to a more stable electrode/solution interface due to doping. This, in turn, is ascribed to the fact that the Mo^{6+} ions tend to concentrate more at the surface, as a result of a synthesis that always includes a necessary calcination, high-temperature stage. This phenomenon of the Mo dopant segregation at the surface in NCM523 material was discovered in the present work for the first time. It appears that Mo doping reduces the reactivity of the Ni-rich NCM cathode materials toward the standard electrolyte solutions of Li-ion batteries. Using density functional theory (DFT) calculations, we showed that Mo^{6+} ions are preferably incorporated at Ni sites and that the doping increases the amount of Ni^{2+} ions at the expense of Ni^{3+} ions, due to charge compensation, in accord with X-ray absorption fine structure (XAFS) spectroscopy measurements. Furthermore, DFT calculations predicted Ni−O bond length distributions in good agreement with the XAFS results, supporting a model of partial substitution of Ni sites by molybdenum.

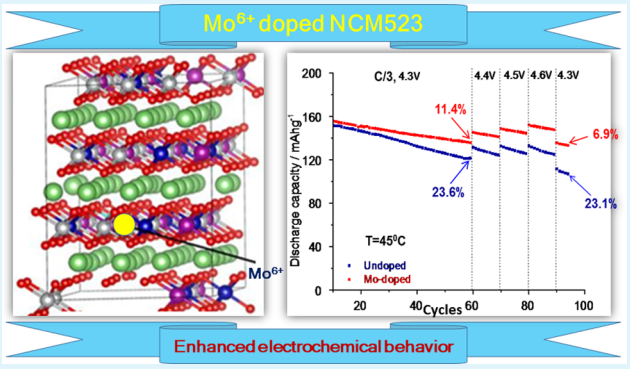

KEYWORDS: *Li-ion batteries, Ni-rich NCM cathodes, Mo^{6+} doping, computational modeling, electrochemical behavior*

1. INTRODUCTION

Lithium-ion batteries (LIB) have attracted much interest since the early 1980s because of the high energy density of Li. They were first introduced into the market by Sony in 1991 to power video cameras. New and more challenging battery requirements, for example electromobility and space technologies, demand significantly improved battery chemistry from all components, including electrodes, electrolyte solutions, and separators. It is widely accepted in the field that in all aspects of modern LIBs, materials for positive electrodes (cathodes) play a dominant role.[1−5] One of the most promising families of cathode materials for batteries in electric vehicles is lithiated oxides of transition metals (TMs) $Li[Ni_xCo_yMn_{1-x-y}]O_2$ (NCM), which can provide good specific capacities that increase with the Ni content and can reach values higher than 200 mAh/g at nickel content around 80% and higher.[5] However, NCM materials suffer from low electronic and ionic conductivities, fast electrode capacity decay, structural instability, and insufficient rate capability.[5]

One of the most successful strategies for improving intrinsic characteristics of cathode materials is lattice doping with cations or anions.[6] Dopants have been found to partially

Received: June 12, 2018
Accepted: August 10, 2018
Published: August 10, 2018

DOI: 10.1021/acsami.8b09795
ACS Appl. Mater. Interfaces 2018, 10, 29608−29621

suppress cation mixing and adverse interfacial reactions. Also, they can stabilize structures of transition metal oxides with or without participating in the redox processes.[7] Dopants can also mitigate unwanted side reactions between the cathode and the electrolyte solutions, thus diminishing the heat evolution from the charged electrodes. A variety of mono- and multivalent dopant ions such as Ag^{+}, Mg^{2+}, Cu^{2+}, Al^{3+}, Cr^{3+}, Fe^{3+}, Ti^{4+}, Zr^{4+}, W^{6+}, and Mo^{6+} were used in LIB cathode materials.[6,8−11] For instance, it was established that a small amount of Al doping in $LiNi_{0.8}Co_{0.2-x}Al_xO_2$ ($0 < x < 0.1$) cathodes significantly stabilized the cell impedance and resulted in enhanced power performance.[12] In a study of double doping of $LiNi_{0.6}Co_{0.2}Mn_{0.2}O_2$ by aluminum and iron, the authors demonstrated that minor contents of the dopants resulted in reduced Li^{+}/Ni^{2+} cation mixing, stabilization of the structure, and enhanced electrochemical behavior of $LiNi_{0.6}Mn_{0.2}Co_{0.15}Al_{0.025}Fe_{0.025}O_2$ cathodes.[13] We have shown recently that Al doping in $LiNi_{0.5}Co_{0.2}Mn_{0.3}O_2$ at a minute level of 0.01 atom % at the expense of all transition metals (i.e., Ni, Co, Mn) resulted in substantial improvements in the electrode performance. This was manifested in reduced capacity fading upon cycling and aging of the cells in a charged state at 60 °C and more stable mean voltage.[14] Using density functional theory (DFT), we identified Ni positions as the most preferred doping sites in NCM523 and also suggested that the Al^{3+} dopant stabilizes the layered structure via strong Al——O iono-covalent bonding because of a significant Al(s)——O(p) overlap, as well as significant charge-transfer capabilities of Al^{3+}.[15] We further investigated the role of doping Ni-rich $LiNi_{0.6}Co_{0.2}Mn_{0.2}O_2$ cathode material by high-charge-state Zr^{4+} cations in a combined experimental and computational study.[16] The Zr-doped electrodes exhibited higher stability, higher rate capability, and lower charge-transfer resistance. It was suggested that the Zr dopants play a 2-fold role in inhibiting layered-to-spinel structural transformation during cycling: destabilization of Ni tetrahedral sites and reducing the number of Jahn−Teller active Ni^{3+} ions. Improved electrochemical performance by doping NCM523 with Zr^{4+} ions was also presented by Wang et al.[17] These authors ascribed the impact of the dopant to reduced cation mixing, enhanced lithium transport kinetics, and lower impedance at a high anodic cutoff voltage of 4.6 V. Recently, it was demonstrated that doping $LiNiO_2$ with Zr^{4+} (0.4 mol %) results in cation ordering and stable electrochemical cycling behavior in the potential range of 2.7−4.3 V.[18]

Doping of cathode materials with high-charge-state cations, such as W^{6+} and Mo^{6+}, was less studied so far, and only a few reports have appeared in the literature.[19−21] It was shown, for instance, that codoping of $LiCoO_2$ with 1 mol % Mn and 1 mol % W results in enhanced electrochemical cycling, increased rate capability and capacity retention, lower charge-transfer resistance, and substantially reduced heat evolution from electrode reactions with solutions.[22] In the case of W^{6+}-doped $LiW_xNi_{0.5}Mn_{1.5-x}O_4$ cathodes, minute doping levels of x = 0.005 demonstrated remarkable capacity retention during cycling, whereas at $x \geq 0.01$, the discharge capacity decreased and the structural stability deteriorated because of abrupt increase in the unit cell volume.[23] Kim et al. recently demonstrated that 1 mol % doping of Ni-rich NCM with W^{6+} results in highly stable LIB prototypes with specific capacities >220 mAh/g because of partial layered-to-cubic (rock salt) phase transition.[24] Molybdenum substitution in Ni-rich materials $LiMo_xNi_{0.8}Mn_{0.1-x}Co_{0.1}O_2$ (x = 0.00, 0.02, 0.04) was shown to suppress the crystal structure change from spinel to rock salt and to improve the thermal stability of the doped samples in reactions with electrolyte solutions.[20] In an earlier work, Sun et al. synthesized Mo-doped $LiMo_xNi_{1/3+x}Co_{1/3}Mn_{1/3-2x}O_2$ ($0 \leq x \leq 0.05$) materials and demonstrated enhanced electrode cyclability in the potential range of 2.8−4.4 V.[19] Studies on Mo^{6+}-modified NCM523 materials were recently performed by Wang et al.[25] These authors established that both Mo doping and surface coating of these materials resulted in improved cycling behavior. They demonstrated that 1 wt % Mo-doped and coated NCM523 exhibited lower capacity fading during prolonged cycling in the potential ranges of 3.0−4.3 and 3.0−4.6 V compared with the unmodified material. On the basis of a number of studies on cation doping in cathode materials, we can conclude that even a minor concentration of dopants (∼1 wt %) effectively stabilizes the structure of cathode materials and the electrode/solution interface and can enhance electrochemical performance.[16,21,25]

Despite the intensive previous work devoted to doped Ni-rich NCM cathodes, Ni-rich materials (Ni ≥ 0.5),[3,6,12−17,19−21,25] more work with dopants like Mo^{6+} cations is required to better understand the correlation between the impact of doping on capacity, stability, and rate capability and possible structural changes induced by the presence of highly charged foreign cations in the lattice of the bulk cathode material. In the present work, we have chosen to work with NCM523 cathode materials because they are considered as the most stable cathode materials in the Ni-rich NCM compound family.[26] Hence, it was interesting to find out if doping at low concentration is effective for a less reactive material. The goal of the work was to gain a better understanding of the impact of Mo^{6+} dopants on this cathode material. We used a variety of sensitive analytical tools and computational efforts in conjunction with electrochemical measurements to obtain a most comprehensive correlation among composition, structure, surface properties, thermal stability, and electrochemical performance. To our knowledge, the above correlation, as well as the phenomenon of Mo^{6+} ion segregation at the surface of NCM523, has never been established or studied.

Whereas in many previous studies the first synthetic step used was coprecipitation of mixed transition metal hydroxide precursors,[27] for this work, we synthesized the precursors (before calcination) by the self-combustion reaction (SCR). Our long-term experience has proven the effectiveness of this synthetic method in preparing precursors with a very uniform distribution of the elements (before the calcination step), especially for the preparation of doped materials.[4,15,16] Despite previous intensive work on doped NCM cathode materials, including a few studies on the use of Mo^{6+} dopants, we believe that the studies described herein take us further in terms of understanding and form an important basis for further studies of Mo-doped NCM cathodes containing very high concentration of Ni (≥0.8).

2. EXPERIMENTAL SECTION

2.1. Synthesis and Characterization of the NCM Materials.

There are several approaches to prepare layered lithiated transition metal oxide cathode materials. In all of the commonly used methods, precursors containing the elements in the right stoichiometry are prepared and then the final stage is always calcination at elevated temperatures in the range 700−900 °C (depending on the

DOI: 10.1021/acsami.8b09795
ACS Appl. Mater. Interfaces 2018, 10, 29608−29621

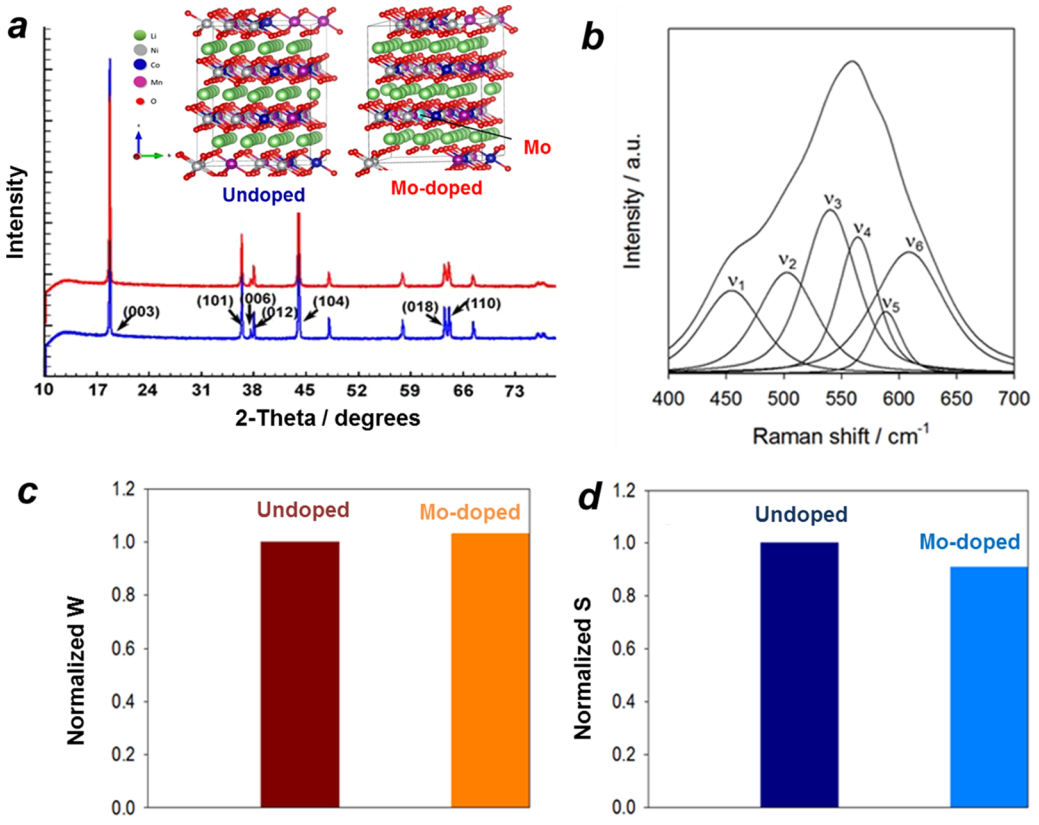

Figure 1. (a) XRD profiles recorded from the NCM523 undoped (blue pattern) and NCM523 Mo-doped (red pattern) pristine materials, showing clear separation of the (108)/(110) and (006)/(102) doublet reflections. Inset: $R\bar{3}m$ structure for undoped NCM523 and Mo-doped NCM523 materials. (b) Typical Raman spectra of NCM523 pristine electrode demonstrating six bands ν_1−ν_6 that correspond to three A_{1g} and three E_g overlapping modes of Ni, Co, and Mn; (c) and (d), respectively, normalized full width at half-maximum (W) and normalized integral areas (S) of ν_4 (A_{1g}) and ν_1 (E_g) bands for Ni measured from Raman spectra of pristine NCM523 undoped and Mo-doped electrodes. The data were analyzed using Renishaw Wire 3.3 software.

composition) in air or under a pure oxygen atmosphere, which forms the final ordered layered structure.[27−30]

On the basis of our previous work, we chose for the present study a simple, low-cost, and effective method based on the self-combustion reaction (SCR).[4,15,16] An appropriate annealing of the product at specified conditions (temperature and time) allows us to obtain submicron- to micron-size particles of the cathode material. Use of this synthetic mode allows fast screening of materials' compositions and their modifications by doping and optimization. $LiNi_{0.5}Co_{0.2}Mn_{0.3}O_2$ undoped and molybdenum-doped materials were produced using the SCR, as described previously.[16] The precursors for the reaction were $LiNO_3$, $Ni(NO_3)_2{\cdot}6H_2O$, $Co(NO_3)_2{\cdot}6H_2O$, and $Mn(NO_3)_2{\cdot}4H_2O$ (Sigma-Aldrich) as oxidizers and sucrose, $C_{12}H_{22}O_{11}$, as fuel. For the synthesis of Mo-doped materials, Li_2MoO_4 was used, by replacing 1% of nickel by molybdenum in the product. The ratio of the fuel and the oxidizer was 2:1. The synthetic procedure is described in more detail in the Supporting Information (SI). The composition of the materials obtained was confirmed by element analysis and corresponds to $LiNi_{0.5}Co_{0.2}Mn_{0.3}O_2$ and $LiNi_{0.49}Co_{0.2}Mn_{0.3}Mo_{0.01}O_2$, respectively. These materials will be referred to as NCM523 undoped and NCM523 Mo-doped in this article. Element analysis of the synthesized materials was carried out using the inductive coupled plasma technique (Ultima-2 spectrometer from Jobin Yvon Horiba). X-ray diffraction (XRD) studies were performed with a Bruker Inc. (Germany) AXS D8 ADVANCE diffractometer in the 2θ range from 10 to 80°, with a step size of 0.01937°, at 1 s/rate. The active surface areas of the materials were measured by the Brunauer, Emmett, and Teller method using Gemini 2375, Micromeritics (multipoint mode). The specific surface areas of the NCM523 undoped and NCM523 Mo-doped materials after annealing at 900 °C were ∼3.2 and ∼4.6 m^2/g, respectively. Their morphology was investigated by a Magellan XHR 400 L FE-SEM-FEI scanning electron microscope with a 15 keV acceleration voltage.

2.2. Transmission Electron Microscopy (TEM) and Electron Diffraction (ED) Measurements. TEM examinations of the materials were performed with a JEOL JEM-2100 (LaB_6) high-resolution electron microscope. Convergent-beam electron diffractions (CBEDs) were taken using a 4−7 nm probe size. Samples for the TEM studies were prepared by a methodology described elsewhere.[31] For the study of possible molybdenum segregationat the surface, the cross sections of the Mo-doped NCM523 material were prepared by a focused ion beam (FIB) using a Helios 600 dual-beam instrument. These samples were then transferred to an FEI Titan scanning/transmission microscope operated at 300 keV for determination of the chemical composition, distribution of the various elements, and high-angle annular dark-field (HAADF) imaging. The elemental analysis was performed using an energy dispersive X-ray spectroscopy (EDS) analyzer with an energy dispersive X-ray analysis (AMETEK Inc.) EDS detector.

2.3. Analysis by Time-of-Flight Secondary-Ion Mass Spectroscopy (TOF-SIMS) and Raman Spectroscopy. TOF-SIMS measurements were performed using two instruments in two independent labs, namely, PHI model 2100 TRIFT II (located at Tel-Aviv University) and ION-TOF GmbH TOF-SIMS 5 (located at the Technion, Israel Institute of Technology). TRIFT II employs a primary Ga/In ion beam and provides a spatial resolution of 120/300 nm. Using TOF-SIMS 5, the depth profiles were taken in a dual mode using 25 keV Bi^+ analysis ions and Cs^+ (for negative secondary's)/O^{2+} (for positive secondary's) as the sputtering ions (incident at 45°). For thin samples, the energy of the O^{2+} ions was 1 keV, whereas for thick samples, the energy was 2 keV. The sputtered area for all

DOI: 10.1021/acsami.8b09795
ACS Appl. Mater. Interfaces 2018, 10, 29608−29621

measurements was 500 × 500 μm^2, and the acquisition area was 100 × 100 μm^2. These measurements were taken from electrodes comprising the 523 Mo-doped materials.

Micro-Raman spectroscopic measurements were performed at room temperature using a micro-Raman spectrometer from Renishaw inVia (U.K.) equipped with a 514 nm laser, a charge-coupled device camera, and an optical Leica microscope, as described previously.[32]

2.4. X-ray Photoelectron Spectroscopy (XPS), X-ray Absorption Near Edge Structure (XANES), and Extended X-ray Absorption Fine Structure (EXAFS) Measurements. X-ray photoelectron spectroscopy (XPS) measurements were performed in ultrahigh vacuum (2.5×10^{-10} Torr base pressure) using a 5600 multi-technique system (PHI). The samples were irradiated with an Al Kα monochromated source (1486.6 eV), and the outcoming electrons were analyzed by a spherical capacitance analyzer using the slit aperture of 0.8 mm in diameter. The samples were not charged during measurements. High-resolution spectra were taken at pass energy of 11.75 eV at increments of 0.05 eV/step to allow precise energy position and peak shape determination. Curve fitting was done with a Gaussian−Lorentzian function using 5600 Multi-Technique System software.

Ni, Co, and Mn K-edge X-ray absorption fine structure (XAFS) spectroscopic measurements, including X-ray absorption near edge structure (XANES) and extended X-ray absorption fine structure (EXAFS), were carried out on the undoped and Mo-doped NCM523 samples. The Mo K-edge XAFS data of the Mo-doped NCM523 sample were measured as well. The samples were ground to fine powder and brushed on tape for measurements. The Ni, Co, and Mn K-edge XAFS data were collected in transmission mode, and Mo K-edge XAFS data were collected in fluorescence mode at Advanced Photon Source 10BM-A,B beamline. The Mo K-edge XAFS of the Li_2MoO_4 standard was measured at Stanford Synchrotron Radiation Lightsource (SSRL) BL2-2 beamline. XAFS data processing and analysis were done using Athena and Artemis software within the IFEFFIT package.[33,34] The normalized k^2-weighted EXAFS data were Fourier transformed in a k range of 2−12 $Å^{-1}$ for Ni, 2−11 $Å^{-1}$ for Mn and Co, and 2.2−11 $Å^{-1}$ for Mo. To fit the Ni, Co, and Mn K-edge EXAFS data, the contributions from metal−oxygen (M−O) and metal−metal (M−M) paths according to the $LiNiO_2$ structure are included. The Mo−O path from the Li_2MoO_4 structure and the Mo−M path from the $LiMO_2$ structure are included to fit Mo K-edge EXAFS of molybdenum-doped NCM523. The values of the amplitude reduction factor (S_0^2) for Co, Ni, Mn, and Mo were obtained from the fitting of the corresponding metal foils and fixed in the fits of the electrode materials.

2.5. Differential Scanning Calorimetry (DSC) Measurements. Details of DSC measurements are provided in the SI.

2.6. Computational Methods. The computational study employed the $R\bar{3}m$ structure of NCM523 layered oxide (Figure 1, inset), as reported in ref 35. This structure contains 60 TMs, and to generate the doped material, we substitute 1 TM by a Mo atom, yielding 1.66% doping of Mo in NCM523, mimicking the experimental doping concentration (1%). All electronic structure calculations were carried out using plane-wave-based DFT, as implemented in the Vienna ab initio simulation package (VASP)[36−38] program. Further computational details can be found in SI.

We note that antiparallel spin transition metal configurations are energetically favorable for both undoped and Mo-doped NCM523, and below we show results for antiferromagnetic configurations only. We have calculated the dopant formation energy (FE) for doping at various sites using the following formula

$$\mathrm{FE} = [E(\mathrm{Mo@NCM523}) + E(\mathrm{M}) + 2E(\mathrm{Li}) + 2E(\mathrm{O_2})] - [E(\mathrm{NCM523}) + E(\mathrm{Li_2MoO_4})]$$

here, E(Mo@NCM) is the energy of Mo-doped NCM523, E(M) is the energy of metal atoms that are replaced by the Mo atom, E(Li) is the energy of the Li atoms, $E(O_2)$ is the energy of an O_2 molecule, E(NCM) is the energy of undoped NCM523, and $E(Li_2MoO_4)$ is the energy of Li_2MoO_4 that is used to introduce Mo into the system.

To compute the intercalation voltages, we have considered the configurations after removing Li atoms from the unit cell according to the range of delithiation and optimized the structures. From the total energy calculations for different limits of delithiation x in Li_x(NCM)-O_2, we have calculated the intercalation voltage from the following formula for both undoped and Mo-doped NCM523[35]

$$V = -\frac{E(\mathrm{Li}_{x+\mathrm{d}x}\mathrm{NCMO_2}) - E(\mathrm{Li}_x\mathrm{NCMO_2})}{\mathrm{d}x} + E(\mathrm{Li_{bcc}})$$

where $E(Li_{x+dx}NCMO_2)$ and $E(Li_xNCMO_2)$ represent the total energy per formula unit of the system before and after lithium deintercalation. $E(Li_{bcc})$ is the energy per formula unit of bulk Li. The Perdew−Burke−Ernzerhof (PBE) functional is known to underestimate the voltage by ca. 1 V for NCM materials.[35] Hence, we apply a rigid shift for all of the PBE voltage values by 1 V, bringing the computed voltages into the experimentally observed range.

2.7. Electrochemical Measurements. Electrochemical tests were carried out in two- and three-electrode cells in 2325 coin-type and pouch-type configurations. The geometric areas of the working electrodes were ∼1.5 and ∼10.5 cm^2 for these cells, respectively. The working electrodes were prepared from mixtures of the active cathode materials, NCM523 undoped or NCM523 Mo-doped, carbon black (Super P from Timcal), KS6 graphite, and poly(vinylidene difluoride) binder (Solef 5130 PVDF), with a ratio of 80:5:5:10 by weight, in *N*-methylpyrrolidone. The slurry was pasted on an aluminum foil (∼20 μm thick, from Strem) using the doctor blade technique. Typical loading of the working electrodes was ∼3−4 mg/cm^2, and counter electrodes of lithium metal were prepared from an ∼200 μm thick foil. Electrochemical cells were assembled in a glove box (VAC) filled with highly pure argon (5 N). The electrolyte solutions (Li battery grade) comprised 1 M $LiPF_6$ dissolved in ethylmethyl carbonate (EMC) and ethylene carbonate (EC), weight ratio 7:3.[16]

3. RESULTS AND DISCUSSION

3.1. Morphological and Structural Characterization of NCM523 Undoped and NCM523 Mo-Doped Materials. According to XRD analysis, the above materials can be considered as a single-phase material based on the rhombohedral phase Li(TM)O_2 with the layered structure of the α-$NaFeO_2$ type belonging to the $R\bar{3}m$ space group. Figure 1a presents a comparison of XRD patterns recorded from the undoped and Mo-doped NCM523 pristine materials (blue and red profiles, respectively). It can be seen that there is essentially no difference between the XRD profiles of undoped and molybdenum-doped materials and that the calculated lattice parameters for both materials are approximately the same, as shown in Table S1. They show the hexagonal structure of the $R\bar{3}m$ space group with a clear separation of the (108)/(110) and (006)/(102) doublet reflections. The full width at half-maximum values correlate with the crystallite sizes of the materials' particles estimated by EVA software and reflect that the Mo-doped particles comprise smaller crystallites compared with the undoped ones. This is in agreement with the averaged particle sizes of 0.64 and 0.41 μm for NCM523 undoped and NCM523 Mo-doped materials, respectively, measured by scanning electron microscopy (Figure S1). It seems that the molybdenum ions affect the size of the particles but have no significant influence on other crystallographic parameters. The lattice parameters and the volume of the unit cell for undoped and doped NCM523 (Mo replacing Ni) were also calculated using DFT (PBE + U + D3) (Table S1), and the absolute values and the trends of the calculated lattice parameters are comparable with experiment. We observe a slight increase in the lattice parameters in the case of Mo-doped NCM523, similar to what is obtained from XRD.

DOI: 10.1021/acsami.8b09795
ACS Appl. Mater. Interfaces 2018, 10, 29608−29621

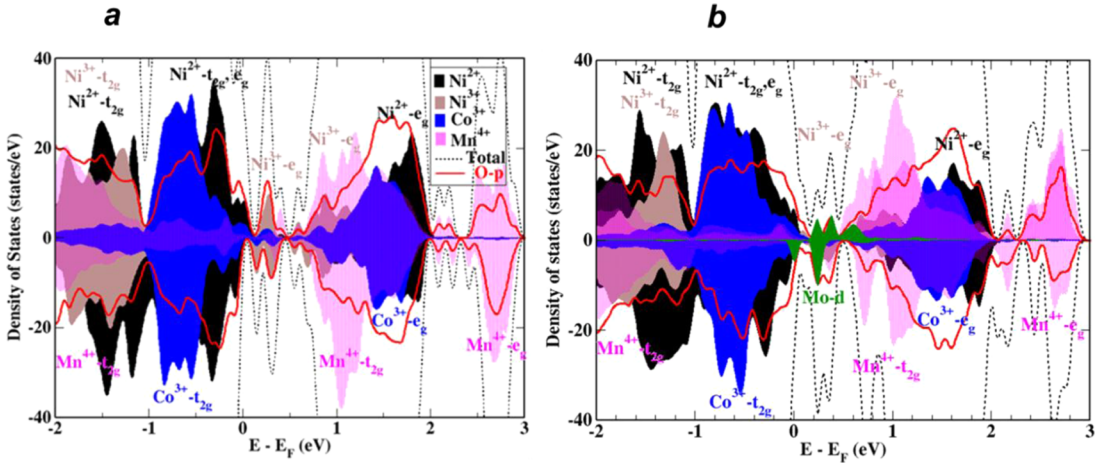

Figure 2. Density of states for undoped (a) and Mo-doped (b) NCM523 samples.

Rietveld refinement (see the Rietveld plot in Figure S2), which was carried out on the XRD data of NCM523 Mo-doped and NCM523 undoped samples, shows that the dopant Mo atoms are distributed solely at the octahedral 3b sites, which are normally occupied by transition metal ions Ni^{2+}, Co^{3+}, and Mn^{4+}. The relationship between the XRD peak intensities obtained from the Rietveld analysis indicates a distinct layered character of the structure of both the undoped and the Mo-doped materials. The observed ratios of peak intensities, $I(003)/I(104)$, were ~1.12 and 1.06 for the undoped and doped materials, respectively, thus providing evidence of good separation of transition metal ions and Li ions into their respective planes in the layered structure,[39,40] while the intensity ratios $(I_{012} + I_{006})/I_{101}$, characterizing the degree of Li/Ni ion mixing within TM cation layers, were ~0.446 and ~0.469 for undoped and Mo-doped samples, respectively.[41,42]

Raman spectroscopy studies of NCM523 undoped and Mo-doped samples also revealed a similar cation mixing of these materials, as discussed below. First, we represent, in Figure 1b, a typical Raman spectrum of a pristine (uncycled) electrode comprising the undoped NCM523 material. This spectrum, obtained by deconvolution (fitting) of the experimental data, demonstrates six bands ν_1–ν_6 that correspond to A_{1g} and E_g Raman-active modes of Ni, Co, and Mn. These modes originate from the metal–oxygen (M–O) symmetrical stretching and oxygen–metal–oxygen (O–M–O) bending vibrations, respectively.[43] In this work, we followed the approach proposed by Julien et al.,[44,45] in which the best fit to the Raman spectra of NCM cathode materials can be achieved taking into account three A_{1g} and three E_g overlapping modes for the three transition metals Ni, Co, and Mn. Thus, bands ν_1 (~450 cm^{-1}), ν_2 (~505 cm^{-1}), and ν_3 (~540 cm^{-1}) are related to E_g modes and bands ν_4 (~560 cm^{-1}), ν_5 (~590 cm^{-1}), and ν_6 (~620 cm^{-1}) are related to A_{1g} modes of Ni, Co, and Mn, respectively. It should be noted that typical Raman spectra measured from the pristine electrode comprising the Mo-doped material are similar to those of undoped samples (Figure 1b). These spectra can also be described as containing overlapping three A_{1g} and three E_g modes centered at comparable positions of ν_1–ν_6 bands. It is possible to estimate the cation mixing between Ni^{2+} and Li^+ in NCM523 undoped and Mo-doped samples from the Raman data. Figure 1c,d compares the normalized full width at half-maxima (W) and normalized integral areas (S) of ν_4 (A_{1g}) and ν_1 (E_g) Raman bands for Ni in undoped and Mo-doped NCM523. The parameters W and S, which reflect the cation mixing in Ni-based lithiated transition metal oxides of layered structure ($R\bar{3}m$ space group), remain almost unchanged with the Mo doping of NCM523, thus indicating comparable levels of cation mixing for undoped and doped samples. This conclusion is in line with the results of the XRD studies, although they reflect bulk properties of the long-range order of the intercalation material, whereas Raman spectroscopy is a short-range-order method relating mostly to the near-surface region of tens or few hundreds nanometers, depending on the penetration depth of the photons into the crystallites.[46,47]

To identify the most stable doping site, we employed DFT as described in the Experimental Section. We substituted the Mo atom at different TM sites, as well as at Li sites. Inspection of the results suggests that Mo doping at Ni^{2+} sites is energetically more favorable than at other metal atom sites or at Li sites (Figure S3), in agreement with the above described experiments.

3.2. Electronic Structure of Undoped and Mo-Doped NCM523 Materials. We further used DFT to elucidate the electronic structure changes due to Mo doping. Our calculated total and partial densities of states (DOS) for geometry-optimized undoped and Mo-doped NCM523 are displayed in Figure 2. As expected, Ni ions are found in different oxidation states, the DOS of Ni lies near the Fermi level, and there is strong hybridization between O p and Ni d, indicating that Ni ions play a major electrochemical role in NCM523. Inspection of Figure 2a reveals that the t_{2g} orbitals of Ni^{2+} are fully occupied (↑↓|↑↓|↑↓), whereas e_g's are partially occupied (↑|↑), indicating that Ni^{2+} is in a high spin (HS) state. t_{2g}'s of Ni^{3+} are fully occupied (↑↓|↑↓|↑↓), and e_g is partially occupied (↑|), in accord with a low spin (LS) state. The Co t_{2g} states are fully occupied (↑↓|↑↓|↑↓), whereas Co e_g are unoccupied (|); hence, we have a Co^{3+} in a LS state. The t_{2g} Mn states are partially filled, i.e., (↑|↑|↑), indicating a HS Mn^{4+} state. Upon 1.66% Mo doping into NCM523, the DOS remains very similar to the DOS for the parent material (Figure 2b), although partially filled Mo d states appear near the Fermi level. However, due to the high oxidation state of Mo (+6) doping, there is a local redistribution of charge of the Ni ions to ensure charge neutrality of the material. This charge

DOI: 10.1021/acsami.8b09795
ACS Appl. Mater. Interfaces 2018, 10, 29608–29621

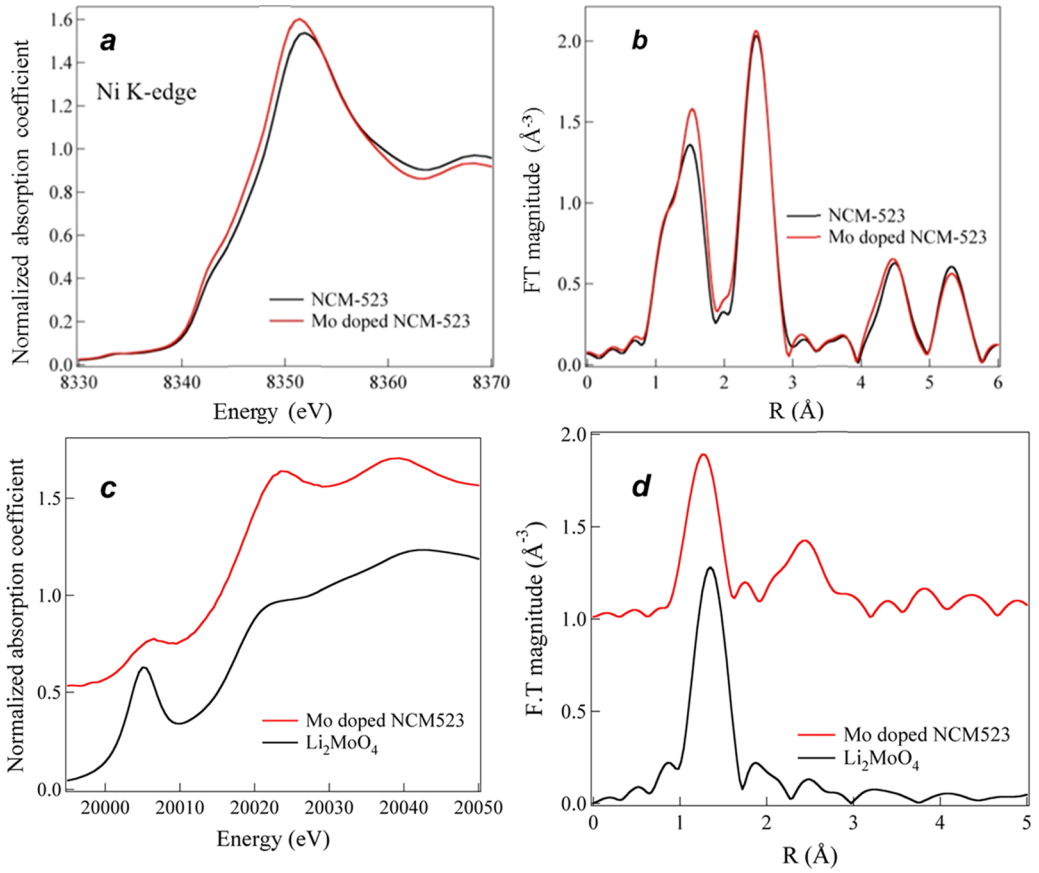

Figure 3. Ni K-edge (a) XANES data and (b) Fourier transform (FT) magnitudes of k^2-weighted EXAFS data of NCM523 and Mo-doped NCM523 samples. Mo K-edge (c) XANES data and (d) FT magnitudes of k^2-weighted EXAFS data of the Mo-doped NCM523 sample compared with the Li_2MoO_4 standard.

distribution of Ni ions in undoped and Mo-doped materials is discussed later.

3.3. EXAFS–XANES and DFT Studies on Undoped and Mo-Doped NCM523 Samples. As seen in Figure 3a, the absorption edge energy of the Mo-doped material at the Ni K-edge is shifted to a slightly lower value compared to that of the undoped material because of Mo^{6+} doping by partial substitution of Ni. The position of the absorption edge energy is related to the charge state of the probed atoms. A linear correlation between the charge state and the energy of edge shift has been constructed using Ni^0 and NiO standards, as reported by O'Grady et al.[48] Here, the position of the absorption edge energy of Mo-doped and undoped materials was measured at half-height position of the edge step where the value of normalized absorption is 0.5, as shown in Table S2. As for Co and Mn K-edge, XANES data of both materials are similar, the doping does not affect the oxidation states of either Co or Mn in these materials, as shown in Figure S4. We then turned to DFT to obtain quantitative information regarding the formal oxidation states of the transition metals. Doping of high-valent Mo (+6) into NCM523 infuses more electrons into the system, and as a result, the charge states of the other ions in the system change. On the basis of our calculations, we identify the magnetic moment per Ni site to deduce the formal oxidation state.[4,16,35,49] Seemingly, the Ni ions are in either a 2+ or a 3+ state in pristine NCM. In Figure 4, we plot the number of Ni^{2+} and Ni^{3+} ions in the unit cell of pristine undoped and Mo-doped NCM523. The percentages of Ni^{2+} (out of all Ni ions) are 63 and 79% for undoped

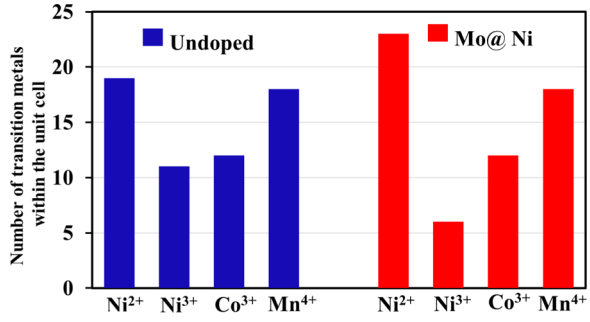

Figure 4. Distribution of Ni^{2+} and Ni^{3+} in undoped and Mo-doped pristine NCM523 materials (PBE + U − D3).

NCM523 and doped Mo@Ni^{2+}, respectively. Doping at the energetically less favorable sites Mo@Co, Mo@Mn, and Mo@Li yields 77, 73, and 80% amounts of Ni^{2+}, respectively. Hence, Mo doping increases the amount of Ni^{2+} ions at the cost of Ni^{3+} ions because of charge compensation. A similar trend is observed with alternative DFT methods PBE and PBE + U + D3 (Figure S4a,b).

Further inspection of our data reveals two major peaks in the Fourier transform (FT) magnitudes of the EXAFS data at the Ni edge (Figure 3b). The first peak corresponds to Ni–O (oxygen) bonds, and the second one to Ni–M (metal) bonds, with only very subtle changes in the peak intensities and their positions in the Ni–O peaks between the undoped and Mo-doped materials. The observed changes are consistent with the slight Ni–O bond distance increase in the Mo-doped material,

DOI: 10.1021/acsami.8b09795
ACS Appl. Mater. Interfaces 2018, 10, 29608–29621

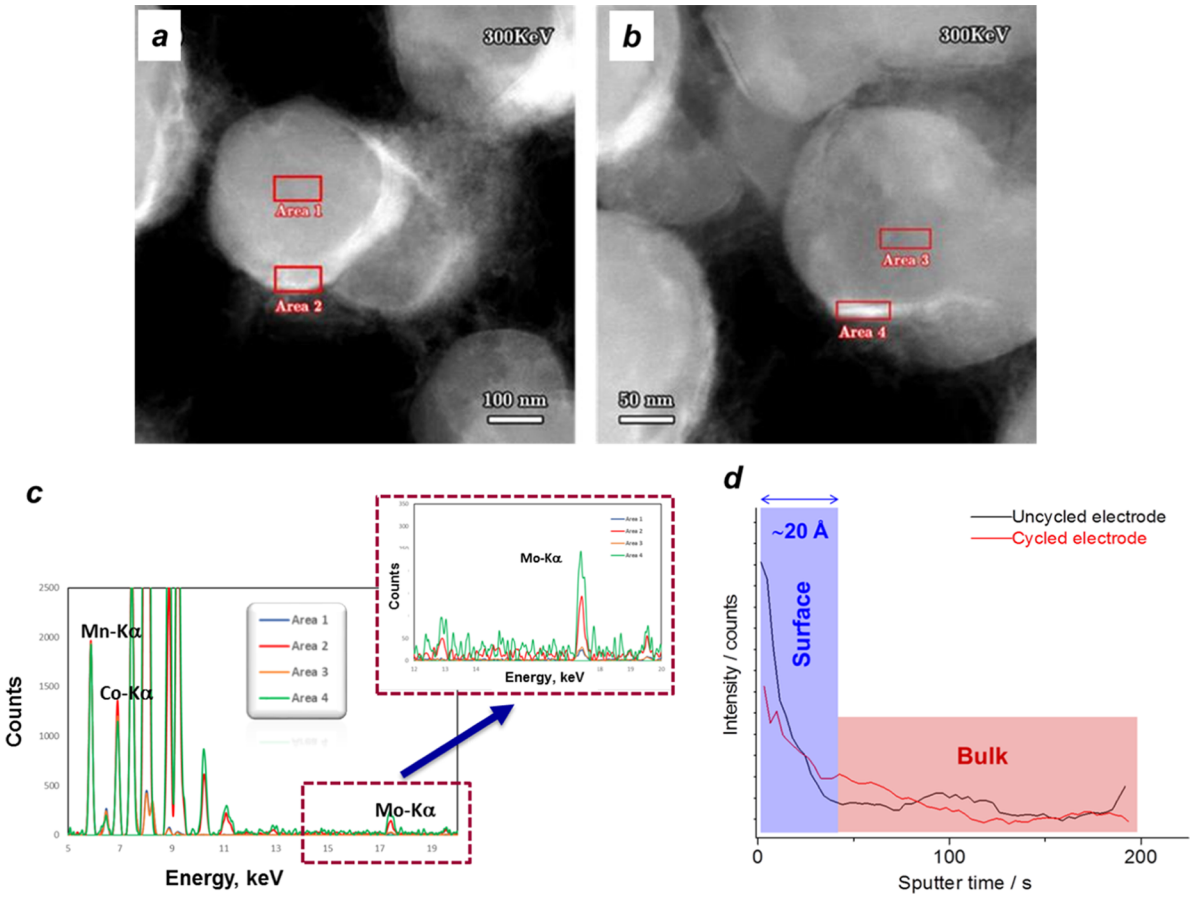

Figure 5. Typical high-resolution TEM images of the Mo-doped NCM523 pristine material measured by HAADF-STEM from several particles at different locations (a) and (b) in the bulk and at the surface indicated as areas (1), (3) and (2), (4), respectively. Samples for HAADF imaging and EDS elemental analysis were prepared by cross sections using the focused ion beam technique. (c) EDS spectra acquired from areas (1)−(4), from which the elemental quantification results are presented in Table S6. Zoom in (c) demonstrates Mo Kα spectra of these areas. (d) TOF-SIMS depth profiles of molybdenum measured from pristine (uncycled) and cycled (as indicated) electrodes comprising NCM523 Mo-doped materials. The electrode was subjected to charge/discharge cycling (90 cycles) and terminated at 2.8 V (discharged state). Due to high roughness of the electrode samples, "surface" and "bulk" are represented schematically, as a guide for the eye.

which is consistent with the observed shift in the XANES data and DFT calculations, which indicate partial reduction of Ni.[48,50] The Ni−O bond distances are shorter for Ni^{3+} compared to those for Ni^{2+} because of the smaller ionic radius in Ni^{3+}. Both Co (bond distances of Co−O and Co−M) and Mn (bond distances of Mn−O and Mn−M) peaks are identical in FT EXAFS data of the undoped and Mo-doped materials, Figure 3c,d. The fitted results of structural parameters of the EXAFS data at Ni, Co, and Mn are shown in Table S3. The average interatomic distance of Ni−O is 1.98 Å for undoped NCM523 and extends to 2.0 Å after Mo doping, as obtained from the fits of Ni K-edge EXAFS data, and this is consistent with visual inspection. The EXAFS data (Figure S5) of Co or Mn K-edge and obtained structural parameters from fitting are very similar for the undoped and Mo-doped samples. Therefore, the observed changes in the charge state of Ni and the interatomic distance of Ni−O are in good agreement with the model of the partial substitution of Ni sites by Mo atoms. We also computed the bond distance distribution using DFT, and based on the current calculations, we observe that the average bond lengths of Ni−O for the undoped and doped cases are 2.018 and 2.036 Å, respectively, in agreement with the trend observed experimentally. The calculations indicate that the distribution of Ni−O distances changes from slightly bimodal to more unimodal due to Mo doping (Figure S6).

The pre-edge position and absorption edge position of Mo K-edge XANES data are quite similar to those for Li_2MoO_4 (Figure 3), and the slight divergence from Li_2MoO_4 may be due to the different local environment. Thus, the charge state of Mo in the sample should be +6. The Fourier transform (FT) magnitudes of k^2-weighted EXAFS data (Figure 3b) provide local structural information, clearly showing that the nearest-neighbor environment around Mo atoms in Mo-doped NCM523 differs from that in the Li_2MoO_4 standard. On the basis of the FT magnitudes of k^2-weighted EXAFS data of Mo-doped NCM523, the first main peak is assigned to the single scattering between Mo and the nearest oxygen neighbors at around 1.5 Å (uncorrected by the photoelectron phase shift), which is similar to the case in the Li_2MoO_4 standard. In addition to the shorter Mo−O contribution, a second major peak (at ∼2.5 Å) is observed, which is absent in Li_2MoO_4. The second neighbors of Mo atoms are likely the transition metals, as a result of Mo atoms substituting for the transition metal atoms in NCM523, and low concentration of Mo. Further quantitative fitting analysis of the EXAFS data at the Mo K-edge was performed by including the Mo−M path (M, transition metal) from the $LiMO_2$ structure. The analysis

DOI: 10.1021/acsami.8b09795
ACS Appl. Mater. Interfaces 2018, 10, 29608−29621

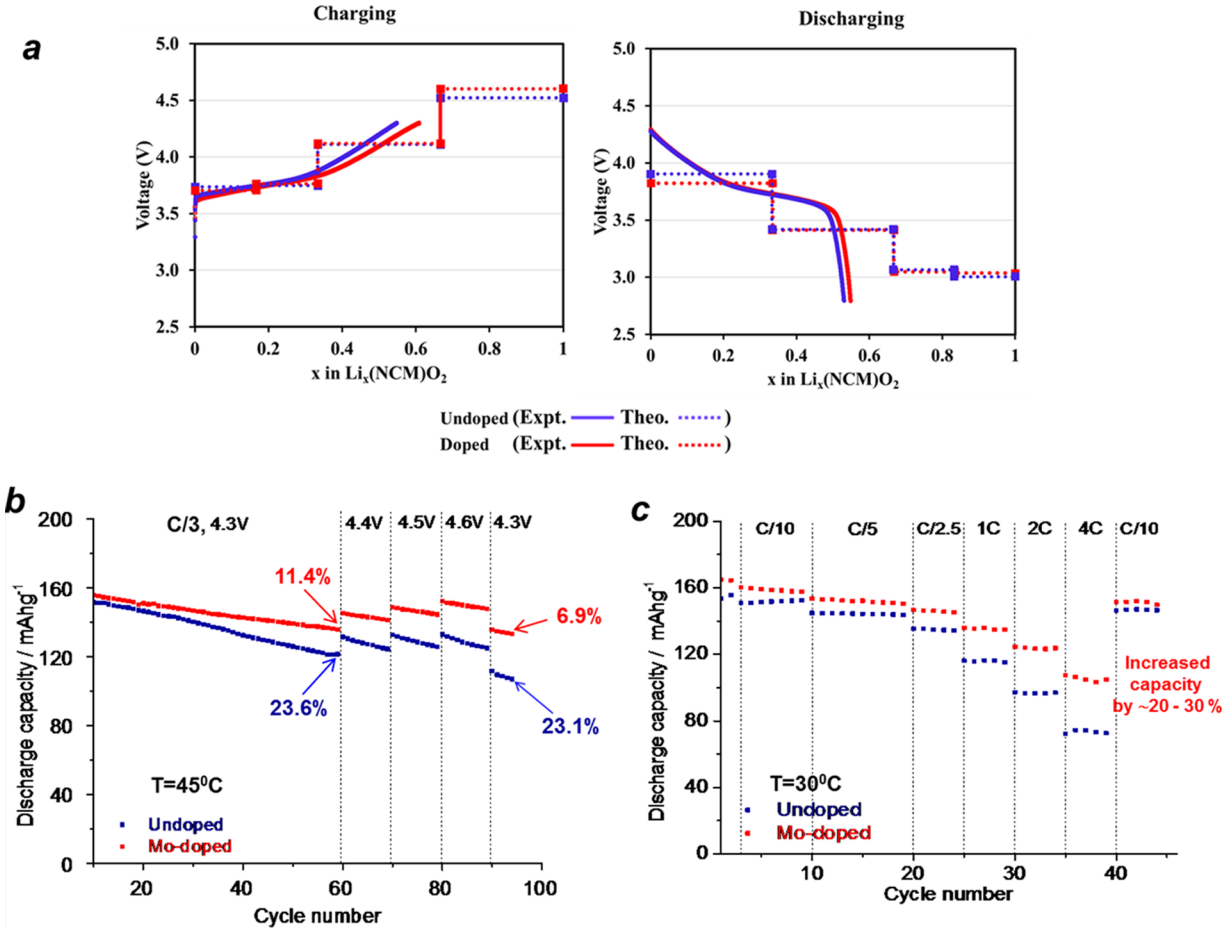

Figure 6. (a) Typical voltage profiles measured from electrodes comprising NCM523 materials, at 30 °C as a function of x in Li$_x$(NiCoMn)O$_2$: undoped (blue solid lines) and Mo-doped (red solid lines), respectively. The anodic cutoff potential was 4.3 V. Dotted lines represent theoretical (modeled) voltage profiles of the above electrodes. (b) Typical cycling performance of electrodes comprising NCM523 undoped and Mo-doped materials at 45 °C (C/3 rate). First formation (conditioning) cycles are not shown. The cutoff potentials and capacity fading values of these electrodes are indicated. Note that Mo-doped electrodes demonstrate much higher capacity retention compared with the undoped ones after cycling to 4.4, 4.5, and 4.6 V. (c) Results of the rate capability tests measured from electrodes comprising NCM523 undoped and Mo-doped materials (30 °C) using constant current mode in the potential range of 2.8−4.3 V.

confirms that the Mo−M contribution corresponds to the second shell in the EXAFS data of Mo-doped NCM523. The fitting results of structural parameters are summarized in Table S4.

In conclusion, the effect of Mo doping in NCM523 is the change in Ni oxidation states and change in the Ni−O bond lengths, as shown clearly from both Ni K-edge EXAFS and XANES data and DFT calculations. These findings are consistent with a model of partial substitution of Ni by Mo^{6+}. The peak intensity increase of the Ni−O peak in the Fourier transform plot of Mo-doped NCM523, with respect to the undoped NCM523 (Figure 3b), is attributed to the lower Ni−O bond length disorder in the doped material (Table S3). This result is in full agreement with the theoretical simulations (Figure S6), showing that the bond length distribution in the doped material is unimodal, whereas in the undoped material, it is bimodal.

3.4. Evidence for Segregation of the Mo^{6+} Dopant at the Surface from EXAFS, TOF-SIMS, and HAADF-STEM−EDS. Above, we demonstrated that molybdenum atoms substitute for nickel atoms in NCM523, and therefore each molybdenum should have six ligating oxygen atoms. However, from the EXAFS fitting results, the coordination number (CN) of Mo−O is 1.3 ± 0.5. This CN suggests that only a fraction of Mo atoms occupy the nickel sites and the remaining ones segregate at the surface. The fraction of all of the molybdenum atoms in the bulk is about $\frac{1.3}{6} = 0.22$, and the fraction of molybdenum atoms segregated at the surface is about $1 - \frac{1.3}{6} = 0.78$. This result is quite close to the observations from HAADF-STEM studies shown in Figure 5. Presented in Figure 5a,b are typical STEM images obtained from cross sections (prepared by FIB cut) of several particles of pristine Mo-doped NCM523, whereas the corresponding EDS results measured at the surface and in the bulk are shown in Figure 5c (EDS spectra) and in Table S5. This data clearly demonstrates that atomic concentrations of Mo detected from the areas 2 and 4 at the surface are significantly higher compared to those in the bulk (areas 1 and 3), indicating segregation of the dopant ions at the surface. Furthermore, segregation was confirmed by measuring the depth profiles of molybdenum by TOF-SIMS from an uncycled (pristine) electrode comprising NCM523 Mo-doped material and that after 90 cycles (Figure 5d). These profiles obviously demonstrate the dopant segregation at the surface of ~20 Å, whereas no segregation was observed for Li, Ni, Mn, and Co in these electrodes, as

DOI: 10.1021/acsami.8b09795
ACS Appl. Mater. Interfaces 2018, 10, 29608−29621

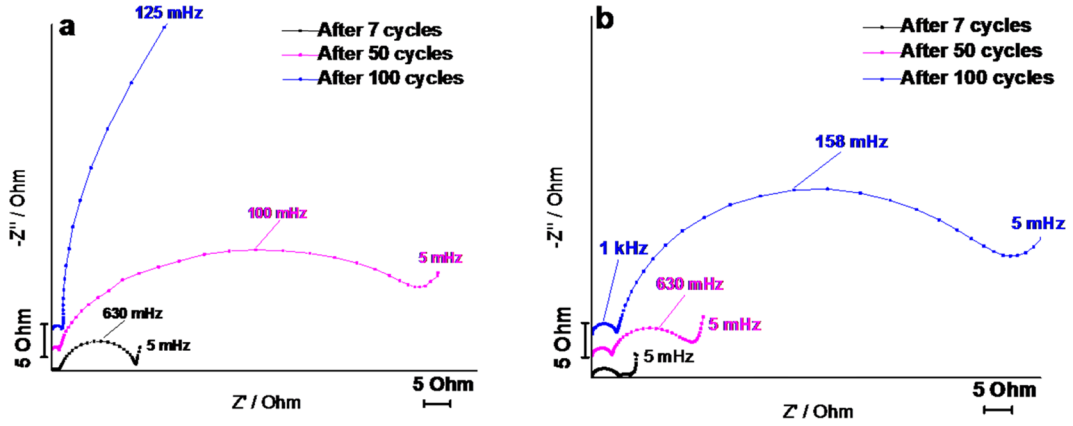

Figure 7. Representative electrochemical impedance spectra measured (30 °C) from electrodes comprising NCM523 undoped (a) and Mo-doped (b) materials in pouch cells, at OCV potential of 3.95 V after seven conditioning (formation) cycles at a C/5 rate and after subsequent 50 and 100 cycles at a C/3 rate. Typically, formation cycles were performed as follows: two at a C/15 rate, two at C/10, and three at C/5. The consecutive cycles were performed at a C/3 rate. Several frequencies are indicated.

follows from Figure S7. Hence, the effective concentration of Mo at the surface is considerably higher than the stoichiometry of the synthesis might indicate. These results are in agreement with those obtained using TOF-SIMS by Manthiram et al.[51] for the segregation of iron, gallium, and chromium dopant ions in spinel samples $LiMn_{1.5}Ni_{0.5-x}M_xO_4$ (M = Cr, Fe, and Ga; x = 0, 0.08). Segregation was also shown by electron energy-loss spectroscopy studies for Al^{3+} and Y^{3+} dopants in ZrO_2, which significantly tend to segregate at the grain boundary interface.[52] Literature reports point to the structural stabilization driven by the surface energy as one of the possible reasons of the dopant segregation at the surface.[53,54] Studies on possible dopant segregation at the surface of high-Ni-content NCM materials (Ni ≥ 0.8) are in progress in our lab, and the results will be reported in a separate paper.

3.5. Effect of Minute Mo Doping on Practical Electrochemical Li Cells with NCM523 Electrodes. In this section, we turn to a comparative electrochemical analysis of undoped and Mo-doped $LiNi_{0.5}Co_{0.2}Mn_{0.3}O_2$ electrodes. Figure 6 demonstrates typical voltage profiles (solid lines) measured from these electrodes, at 30 °C with the anodic cutoff potential of 4.3 V. The theoretical profiles obtained from DFT calculations are also shown (dotted lines) in this figure and show excellent agreement between the experimental and theoretical trends. Both the electrodes (undoped and Mo-doped) demonstrate discharge capacity of around 160 mAh/g in the first few formation cycles, which decreases to ∼150−140 mAh/g during subsequent cycling at a C/3 rate. The irreversible capacity loss (ICL) values in the first cycle were ∼9.4 and ∼7.1% for undoped and Mo-doped electrodes, respectively (as averaged from seven cells running in parallel, for statistical purpose). Slightly lower ICL for the Mo-doped samples may be related to lesser side reactions of these electrodes with electrolyte solutions because of the Mo^{6+}-modified electrode/solution interface. We suggest that the effect of modification can be related partially to a stable "dopant−oxide monolayer" formed on the surface.[55] An indirect evidence of the modified interface of Mo-doped samples was demonstrated by our differential calorimetry studies discussed below.

From the electrochemical testing results, we conclude that Mo-doped electrodes demonstrate also more stable behavior (lower capacity fading) during cycling to 4.3 V, as well as to higher cutoff potentials of 4.4, 4.5, and 4.6 V both at 30 °C (Figure S8) and at the elevated temperature of 45 °C (Figure 6b). At this temperature, the Mo-doped electrodes exhibit lower capacity fading and much higher capacity retention compared to those of their undoped counterparts. An advantageous electrochemical performance of the Mo-doped samples is evident from their rate capability measurements that exhibit ∼20−30% higher capacities at 1C−4C rates compared to those of the undoped ones, as indicated in Figure 6c. This can be attributed to faster kinetics of electrodes comprising NCM523 Mo-doped material. Similar data on the advantageous rate capability of 1 wt % Mo-doped NCM523 electrodes was demonstrated recently by Zhang et al.[21] From the results of voltammetric measurements of undoped and doped electrodes at a slow potential scan rate of 50 μV/s in Figure S9, we also conclude that the doped electrodes possess faster kinetics. Indeed, they exhibit larger anodic and cathodic peak currents in cyclic voltammograms (normalized by the active mass) and much lower difference between anodic and cathodic peak potentials (peak-to-peak separation), $\Delta = E_{an} - E_{cath} = 60$ mV. This value is very close to the theoretical one of 59 mV of reversible one electron transfer[56] and is much lower compared to Δ = 210 mV for the undoped ones. Although cyclic voltammetries (CVs) (Figure S9) reflect complex behavior of the NCM electrodes upon charging/discharging, including redox reactions like $Ni^{2+}/Ni^{3+}/Ni^{4+}$ and Co^{3+}/Co^{4+} and possible phase transitions (which are typically not observed for modestly Ni-enriched NCM523 but become pronounced for compositions with Ni >0.6),[57] a slow-enough cycling at quasi-equilibrium conditions illustrates a faster kinetics of the Mo-doped electrodes. This conclusion is supported by a comparative analysis of electrochemical impedance spectra of undoped and Mo-doped electrodes (Figure 7a,b) measured at open-circuit voltage (OCV) potential of 3.95 V during prolonged cycling (i.e., namely, after seven conditioning (formation) cycles and after consequent 50 and 100 cycles at a C/3 rate and 30 °C). These spectra are characterized by two semicircles at high (100 kHz to 10 Hz) and medium (tens of hertz) frequencies, respectively, and a "tail-like" feature at very low frequencies (millihertz range). These spectra are typical for NCM Li-intercalation electrodes.[16,19] The first semicircle is usually related to the resistance of Li ion migration through the surface films formed on the electrodes, whereas the second

DOI: 10.1021/acsami.8b09795
ACS Appl. Mater. Interfaces 2018, 10, 29608−29621

semicircle is ascribed to the interfacial charge-transfer resistance (R_{ct}), and a tail-like feature (Warburg impedance) at very low frequencies is related to the Li^+ solid-state diffusion. Here, we demonstrate much lower charge-transfer resistance, R_{ct}, for the doped electrodes during cycling measured upon charging from 3.7 to 4.3 V (Figure S10). It is important to emphasize that R_{ct} increases rapidly with cycling of the undoped NCM523 electrodes, whereas it is only slightly changed for Mo-doped samples, which can be ascribed to the modified stable interface comprising segregated Mo^{6+} ions. We hypothesized that segregated Mo^{6+} ions lower the charge-transfer resistance because of the additional conduction bands near the Fermi level (Figure 2b), which may facilitate the transfer of Li ions and electrons, as a result, increasing the exchange current density and decreasing the charge-transfer resistance, according to the Butler–Volmer equation.[58] Similar results of the improved Li-ion transport and more stable electrode/solution interface due to doping (by Mo and W) and W-segregation were also established in Mo^{6+}-doped TiO_2 nanocrystals[59] and in W-doped spinel $LiMn_{1.5}Ni_{0.5}O_4$.[60]

Indirect evidence of the modified interface comes from differential scanning calorimetry measurements, which reveal that the total heat (Q_t) evolved in the reactions of the NCM523 Mo-doped material with the EC–EMC/$LiPF_6$ solution is ~2 times lower than that in the undoped material, with values of Q_t = 116 and 210 J/g, respectively.

It is noticeable that the Mo-doped electrodes attain electrochemically stable behavior even after the first cycle, whereas the undoped cathodes stabilize only after a few CV cycles (Figure S9b,c). Overall, we conclude that these experimental observations agree quite well with those in our previous work on Zr^{4+}-doped NCM622 electrodes,[16] with results of Mo-modified NCM523 electrodes presented by Wang et al.[21] and with suggestions on the modified stable interface developed in cation-doped or surface-coated $LiCoO_2$ and NCM333 electrodes studied recently by Ogumi et al.[61,62]

3.6. XPS Analysis of Mo-Doped NCM523 Electrodes. The chemical changes in Mo before and after cycling of doped electrodes (80 cycles, terminated in discharged state) were characterized by XPS. The comparison of cycled and uncycled electrode surfaces is presented in Figure 8a and demonstrates a very complex spectral structure following electrode cycling. Inspection of the Mo 3d curve-fitted spectra of both electrodes shows the Mo $3d_{5/2}$ and Mo $3d_{3/2}$ peaks of the fitted doublets, with a fixed peak splitting of 3.13 eV between them. The most pronounced Mo $3d_{5/2}$ component in the fitted spectrum of the uncycled electrode is observed at 232.1 eV. Although numerous references for Mo oxides are rather contradictory, most of them suggest a MoO_3 peak position at an energy no higher than ca. 232.1–232.6 eV.[63–65] Hence, the peak at 232.1 eV, revealed in both uncycled and cycled electrodes, is attributed to MoO_3. After cycling, in addition to Mo^{6+} (Mo $3d_{5/2}$ peak at 232.1 eV), there is also an Mo^{5+} component (Mo $3d_{5/2}$ peak at 231.6 eV, Figure 8c) that points to Mo^{6+} reduction related to electrode cycling. This finding is in line with the DFT calculations, which showed Mo conduction states located near the Fermi level (Figure 2b). Two other Mo $3d_{5/2}$ components at higher binding energies of 233.4 and 234.3 eV (Figure 8c) suggest O–Mo–F and F–Mo–F bonding, respectively, which is possibly due to interactions with $LiPF_6$ from the electrolyte and the PVDF binder.

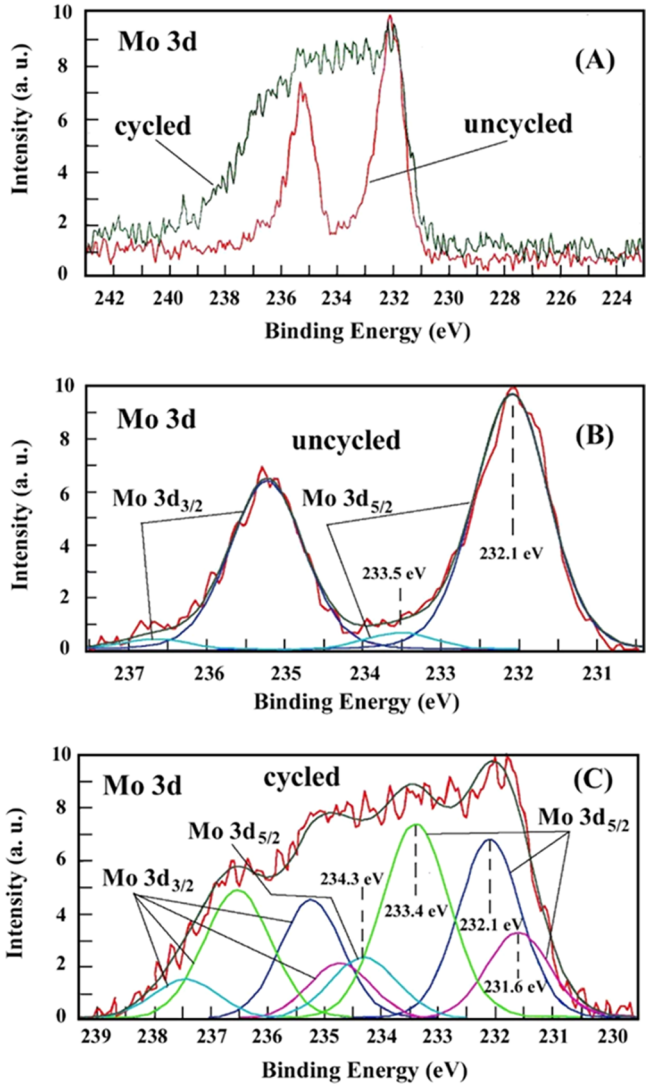

Figure 8. XPS analysis of Mo 3d spectra measured from electrodes comprising NCM523 doped materials. Comparison of Mo 3d spectra of cycled (80 cycles terminated in the discharged state, 2.8 V) and uncycled samples (A). Curve-fitted spectra of uncycled (B) and cycled (C) samples with indication of the Mo $3d_{3/2}$ and Mo $3d_{5/2}$ components and the binding energy values of the Mo $3d_{5/2}$ peaks. Cycling was carried out in coin-type cells filled with EC/EMC (7:3)/$LiPF_6$ solutions at a C/3 rate, 30 °C.

In the following section, we discuss the structural transformations occurring in the undoped and Mo-doped NCM523 materials during cycling and at different states-of-charge.

3.7. Structural Transformations in Undoped and Mo-Doped NCM523 Materials during Electrochemical Cycling. Changes in the XRD patterns in the Mo-doped material produced by charge/discharge cycling (90 cycles) with final charging to 4.3 V and by cycling ended by discharging to 2.8 V are presented in Figure S11. Although the original rhombohedral structure of the material is retained, we observe a noticeable shift of the diffraction peaks in the profile (in red) corresponding to cycling terminated by charging to 4.3 V. The peaks (101) and (104) move to higher angles, thus indicating that the *a*-parameter contracts during charging.

This is apparently caused by the delithiation process in the course of the final charging to 4.3 V. It should be noted,

DOI: 10.1021/acsami.8b09795
ACS Appl. Mater. Interfaces 2018, 10, 29608–29621

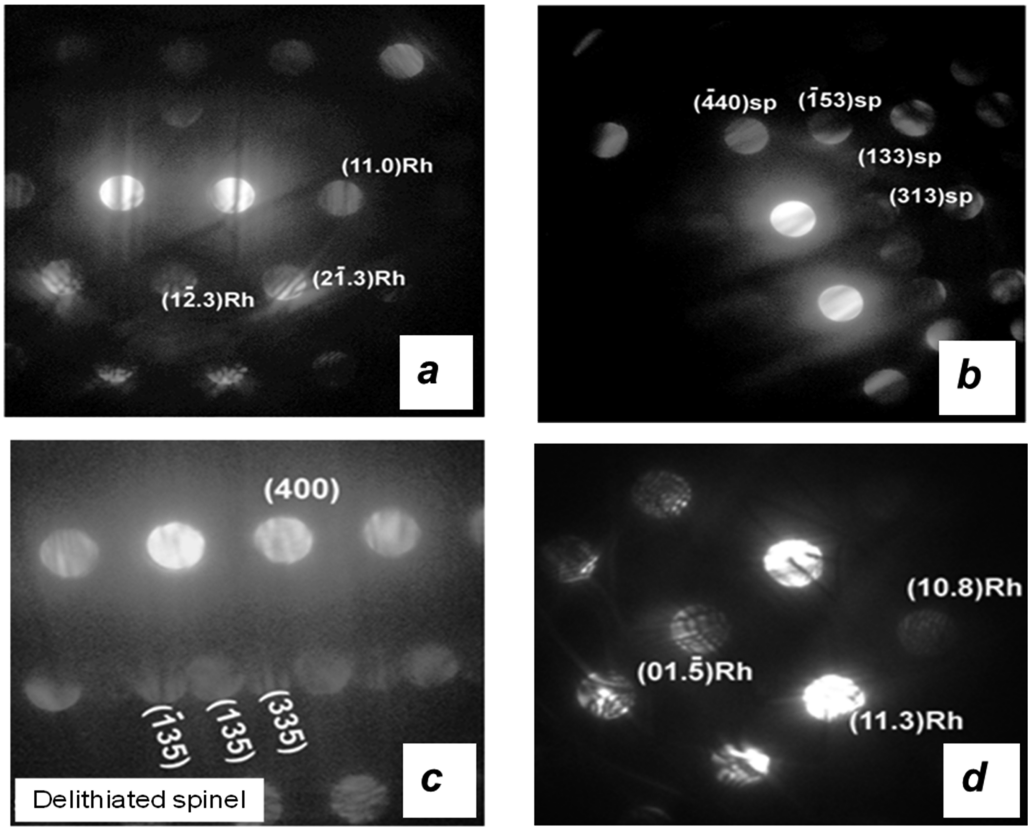

Figure 9. (a, b) Indexed nanobeam electron diffraction patterns taken, respectively, from 2 particles of the NCM523 Mo-doped electrode subjected to charge/discharge cycling (90 cycles) terminated by discharging to 2.8 V. (c) and (d) patterns, respectively, taken from peripheral and inner areas of the particle of the cycled NCM523 undoped material. The electrode was subjected to charge/discharge cycling (90 cycles) and terminated at 2.8 V (discharged state). "Rh" and "sp" denote the rhombohedral and spinel phases, respectively.

however, that peak (003) does not shift, suggesting that the *c* parameter does not change.

When the electrochemical cycling is completed by subsequent discharge, lithium ions intercalate back to their octahedral sites within the layered structure and the unit cell dimensions are restored approximately to their initial values, which is manifested by shifting diffraction peaks back toward their former positions. Table S6 shows the results of least-squares refinement of the lattice parameters characterizing "charge" and "discharge" cases. It follows from Table S6 that if cycling is terminated by charging to 4.3 V, the unit cell volume of the cycled material decreases, apparently due to extraction of lithium during the final charging. Correspondingly, the *a* lattice parameter decreases because the distance between the transition metal ions is reduced as a result of their oxidation, albeit the *c* lattice parameter remains largely unchanged. When the lithium ions intercalate to the structure during the final discharge performed after charge/discharge cycling, the unit cell volume is restored almost completely (compare with Table S1).

We have previously shown that NCM523 undergoes layered-to-spinel transformation on cycling.[14] The XRD patterns of the cycled layered Mo-doped NCM523 samples did not contain direct evidence of transformation to the spinel phase LiM_2O_4, but the reduced spacing between the peaks (006)/(012) after cycling, as compared to the easily distinguishable (006)/(102) doublet in the pristine, nevertheless, may suggest the formation of spinel. TEM examinations of individual particles of the cycled materials confirm this suggestion (Figure 9). The presence of cubic spinel was revealed both in the cycled Mo-doped NCM523 samples that were charged to 4.3 V and in those discharged to 2.8 V.

Figure 9a,b shows a pair of convergent-beam electron diffraction (CBED) patterns taken from two particles of Mo-doped NCM523 after cycling, terminated by discharging to 2.8 V. Whereas the pattern in Figure 9a,b was interpreted on the basis of the rhombohedral phase $LiMO_2$, the pattern in Figure 9a,b could only be indexed in terms of cubic spinel. In samples subjected to charge/discharge cycling (90 cycles) terminated by charging to 4.3 V, we observed completely delithiated spinel Mn_2O_4. The representative selected-area diffraction pattern taken from the cycled Mo-doped material charged to 4.3 V is shown in Figure S13a. This diffraction pattern contains two superimposed reflection systems: one (intensive reflections) is related to the original rhombohedral $Li(TM)O_2$ phase and the other (weak reflections) is ascribed to delithiated spinel Mn_2O_4. The dark-field image (Figure S13b) taken with Mn_2O_4 reflection clearly shows that the nanoparticles of the Mn_2O_4 phase are distributed at the periphery of the particle.

For comparison, the undoped NCM523 cycled material was also analyzed by TEM. Figure 9c demonstrates the nanobeam diffraction pattern showing the presence of the cubic delithiated spinel Mn_2O_4 in the particle of the cycled undoped NCM523 material, which was cycled and terminated by discharging to 2.8 V. The spinel pattern was obtained only from the peripheral area of the particle; the structure of the inner region of the particle was rhombohedral, as shown in Figure 9d. Apparently, the process of transformation of the

DOI: 10.1021/acsami.8b09795
ACS Appl. Mater. Interfaces 2018, 10, 29608−29621

rhombohedral phase to a spinel structure begins at the periphery of the grain (at the surface) and progresses toward its internal part. These observations are in agreement with our work on NCM622 Zr-doped electrodes[16] and with the recent studies by Doeff et al.[66,67] on structural reconstruction and chemical evolution of NCM materials, emphasizing thus the importance of the surface phenomena and phase transitions occurring in Ni-rich cathodes during cycling.

4. CONCLUSIONS

In this work, undoped and 1 mol % molybdenum-doped $LiNi_{0.5}Co_{0.2}Mn_{0.3}O_2$ lithium-ion battery cathode materials were synthesized using a self-combustion reaction. We performed "in situ" cationic doping, employing the precursors Li, Ni, Co, and Mn nitrates (oxidizers) and sucrose (fuel) and Li_2MoO_4 as the molybdenum source. On the basis of DFT calculations, we conclude that Mo replaces Ni ions at 3b sites and even minor Mo doping increases the amount of Ni^{2+} ions in NCM523 at the cost of Ni^{3+} ions because of charge compensation. Analysis of both Ni K-edge EXAFS and XANES data and DFT calculations led us to conclude that doping affects Ni oxidation states and Ni−O bond lengths. These findings are consistent with a model of partial substitution of Ni by Mo^{6+}. An additional important finding of this work is that the Mo^{6+} ions tend to segregate at the surface, a phenomenon we established for the first time in NCM523 materials.

We established reduced capacity fading of Mo-doped electrodes during cycling to 4.3 V and to higher cutoff potentials of 4.4−4.6 V both at 30 °C and at the elevated temperature of 45 °C and concluded that Mo-doped electrodes exhibited ∼20−30% higher rate capability at 1C−4C rates, which may be attributed to faster kinetics of these cathode materials. This was confirmed, in particular, by analysis of the measured charge-transfer resistance values calculated from impedance spectra of undoped and doped electrodes during consecutive cycling (up to 100 cycles). This kinetic parameter was shown to increase rapidly with cycling of undoped electrodes, whereas it changed only slightly for Mo-doped ones, and this can be ascribed to the modified stable interface comprising segregated Mo^{6+} ions. Indirect evidence of the modified interface was also obtained from studies of thermal behavior of NCM523 materials. They allow us to conclude that NCM523 Mo-doped samples demonstrate ∼2 times lower total heat evolved in reactions with the EC−EMC/$LiPF_6$ battery solution (Q_t = 116 J/g) in comparison with the undoped ones (Q_t = 210 J/g). This reduced heat evolution implies less interaction with the solution species such as trace water, PF_5, hydrofluoric acid (contaminants related to $LiPF_6$), and the alkyl carbonate solvents in the temperature range of 30−300 °C.

By analyzing the nanobeam electron diffraction patterns obtained from TEM studies of several individual particles of the cycled NCM523 electrode materials, we conclude that both undoped and Mo-doped samples form some cubic spinel phase. These cubic spinel phases that were detected in discharged and charged electrodes are likely $Li(TM)_2O_4$ or delithiated Mn_2O_4, respectively. The above partial structural layered-to-spinel transformation was detected mainly at the periphery of the grains, and it progresses toward the bulk of the particles.

We also note that surface-sensitive XPS studies of cycled Mo-doped electrodes terminated in a discharged state, revealing the presence of Mo^{5+} ions in addition to Mo^{6+}. This fact can be ascribed to Mo^{6+} reduction related to electrode cycling and agrees with the DFT calculations, which showed molybdenum conduction band states located near the Fermi level.

In summary, in this combined theoretical and experimental study, we address the questions related to the structural, surface, and electronic characteristics and electrochemical performance of undoped and Mo-doped $LiNi_{0.5}Co_{0.2}Mn_{0.3}O_2$ cathodes. We conclude that doping of these cathode materials with the highly charged cation Mo^{6+} (even at a minute level) is a promising path toward enhancing electrochemical activity in advanced lithium-ion batteries.

■ ASSOCIATED CONTENT

Supporting Information

The Supporting Information is available free of charge on the ACS Publications website at DOI: 10.1021/acsami.8b09795.

Synthesis and characterization of the NCM523 materials; their analysis by time-of-flight secondary-ion mass spectroscopy and Raman spectroscopy, differential scanning calorimetry, computational methods, and electrochemical techniques; and also, structural transformations in undoped and Mo-doped NCM523 materials during electrochemical cycling (PDF)

■ AUTHOR INFORMATION

Corresponding Author

*E-mail: aurbach@mail.biu.ac.il.

ORCID

Anatoly I. Frenkel: 0000-0002-5451-1207
Dan T. Major: 0000-0002-9231-0676
Boris Markovsky: 0000-0001-7756-0071
Doron Aurbach: 0000-0001-8047-9020

Notes

The authors declare no competing financial interest.

■ ACKNOWLEDGMENTS

D.A. and D.T.M. acknowledge support from the Israel Committee for High Education and the Israel Prime Minister Office in the framework of the INREP project. A.I.F. and J.L. acknowledge support by the U.S. National Science Foundation Grant No. CHE-1719534. Synchrotron characterization used resources of the Advanced Photon Source and Stanford Synchrotron Radiation Lightsource, the U.S. Department of Energy (DOE) Office of Science User Facilities. MRCAT beamline operations are supported by the Department of Energy and the MRCAT member institutions. BL2-2 beamline of the SSRL was supported in part by the Synchrotron Catalysis Consortium (U.S. Department of Energy, Office of Basic Energy Sciences, grant no. DE-SC0012335). Financial support by the BASF SE through its Research Network on Electrochemistry and Batteries is gratefully acknowledged. B.M. acknowledges Dr. Susai F. Amalraj from Bar-Ilan University and Prof. David Fucks from Ben-Gurion University of the Negev, Israel, for helpful discussions.

■ REFERENCES

(1) Marom, R.; Amalraj, S. F.; Leifer, N.; Jacob, D.; Aurbach, D. A Review of Advanced and Practical Lithium Battery Materials. *J. Mater. Chem.* **2011**, *21*, 9938−9954.

(2) Yu, X.; Lyu, Y.; Gu, L.; Wu, H.; Bak, S.-M.; Zhou, Y.; Amine, K.; Ehrlich, S. N.; Li, H.; Nam, K.-W.; Yang, X.-Q. Understanding the

DOI: 10.1021/acsami.8b09795
ACS Appl. Mater. Interfaces 2018, 10, 29608−29621

Rate Capability of High-Energy-Density Li-Rich Layered $Li_{1.2}Ni_{0.15}Co_{0.1}Mn_{0.55}O_2$ Cathode Materials. *Adv. Energy Mater.* **2014**, *4*, No. 1300950.
(3) Andre, D.; Kim, S.-J.; Lamp, P.; Lux, S. F.; Maglia, F.; Paschos, O.; Stiaszny, B. Future Generations of Cathode Materials: An Automotive Industry Perspective. *J. Mater. Chem. A* **2015**, *3*, 6709−6732.
(4) Schipper, F.; Nayak, P.; Erickson, E.; Amalraj, S.; Srur-Lavi, O.; Penki, T.; Talianker, M.; Grinblat, J.; Sclar, H.; Breuer, O.; Julien, C.; Munichandraiah, N.; Kovacheva, D.; Dixit, M.; Major, D.; Markovsky, B.; Aurbach, D. Study of Cathode Materials for Lithium-Ion Batteries: Recent Progress and New Challenges. *Inorganics* **2017**, *5*, No. 32.
(5) Ryu, H.-H.; Park, K.-J.; Yoon, C. S.; Sun, Y.-K. Capacity Fading of Ni-Rich $Li[Ni_xCo_yMn_{1-x-y}]O_2$ ($0.6 \leq x \leq 0.95$) Cathodes for High-Energy-Density Lithium-Ion Batteries: Bulk or Surface Degradation? *Chem. Mater.* **2018**, *30*, 1155−1163.
(6) Fergus, J. W. Recent Developments in Cathode Materials for Lithium ion Batteries. *J. Power Sources* **2010**, *195*, 939−954.
(7) Myung, S.-T.; Maglia, F.; Park, K.-J.; Yoon, C. S.; Lamp, P.; Kim, S.-J.; Sun, Y.-K. Nickel-Rich Layered Cathode Materials for Automotive Lithium-Ion Batteries: Achievements and Perspectives. *ACS Energy Lett.* **2017**, *2*, 196−223.
(8) Pouillerie, C.; Perton, F.; Biensan, P.; Pérès, J. P.; Broussely, M.; Delmas, C. Effect of Magnesium Substitution on the Cycling Behavior of Lithium Nickel Cobalt Oxide. *J. Power Sources* **2001**, *96*, 293−302.
(9) Huang, B.; Li, X.; Wang, Z.; Guo, H.; Xiong, X. Synthesis of Mg-doped $LiNi_{0.8}Co_{0.15}Al_{0.05}O_2$ Oxide and its Electrochemical Behavior in High-voltage Lithium-ion Batteries. *Ceram. Int.* **2014**, *40*, 13223−13230.
(10) Du, R.; Bi, Y.; Yang, W.; Peng, Z.; Liu, M.; Liu, Y.; Wu, B.; Yang, B.; Ding, F.; Wang, D. Improved Cyclic Stability of $LiNi_{0.8}Co_{0.1}Mn_{0.1}O_2$ via Ti Substitution with a Cut-off Potential of 4.5 V. *Ceram. Int.* **2015**, *41*, 7133−7139.
(11) Hu, G.; Zhang, M.; Liang, L.; Peng, Z.; Du, K.; Cao, Y. Mg−Al−B co-substitution $LiNi_{0.5}Co_{0.2}Mn_{0.3}O_2$ Cathode Materials with Improved Cycling Performance for Lithium-ion Battery under High Cutoff Voltage. *Electrochim. Acta* **2016**, *190*, 264−275.
(12) Chen, C. H.; Liu, J.; Stoll, M. E.; Henriksen, G.; Vissers, D. R.; Amine, K. Aluminum-doped Lithium Nickel Cobalt Oxide Electrodes for High-power Lithium-ion Batteries. *J. Power Sources* **2004**, *128*, 278−285.
(13) El Mofid, W.; Ivanov, S.; Konkin, A.; Bund, A. A High Performance Layered Transition Metal Oxide Cathode Material Obtained by Simultaneous Aluminum and Iron Cationic Substitution. *J. Power Sources* **2014**, *268*, 414−422.
(14) Aurbach, D.; Srur-Lavi, O.; Ghanty, C.; Dixit, M.; Haik, O.; Talianker, M.; Grinblat, Y.; Leifer, N.; Lavi, R.; Major, D. T.; Goobes, G.; Zinigrad, E.; Erickson, E. M.; Kosa, M.; Markovsky, B.; Lampert, J.; Volkov, A.; Shin, J.-Y.; Garsuch, A. Studies of Aluminum-Doped $LiNi_{0.5}Co_{0.2}Mn_{0.3}O_2$: Electrochemical Behavior, Aging, Structural Transformations, and Thermal Characteristics. *J. Electrochem. Soc.* **2015**, *162*, A1014−A1027.
(15) Dixit, M.; Markovsky, B.; Aurbach, D.; Major, D. T. Unraveling the Effects of Al Doping on the Electrochemical Properties of $LiNi_{0.5}Co_{0.2}Mn_{0.3}O_2$ Using First Principles. *J. Electrochem. Soc.* **2017**, *164*, A6359−A6365.
(16) Schipper, F.; Dixit, M.; Kovacheva, D.; Talianker, M.; Haik, O.; Grinblat, J.; Erickson, E. M.; Ghanty, C.; Major, D. T.; Markovsky, B.; Aurbach, D. Stabilizing Nickel-rich Layered Cathode Materials by a High-charge Cation Doping Strategy: Zirconium-doped $LiNi_{0.6}Co_{0.2}Mn_{0.2}O_2$. *J. Mater. Chem. A* **2016**, *4*, 16073−16084.
(17) Wang, D.; Li, X.; Wang, Z.; Guo, H.; Xu, Y.; Fan, Y.; Ru, J. Role of Zirconium Dopant on the Structure and High Voltage Electrochemical Performances of $LiNi_{0.5}Co_{0.2}Mn_{0.3}O_2$ Cathode Materials for Lithium ion Batteries. *Electrochim. Acta* **2016**, *188*, 48−56.
(18) Yoon, C. S.; Choi, M.-J.; Jun, D.-W.; Zhang, Q.; Kaghazchi, P.; Kim, K.-H.; Sun, Y.-K. Cation Ordering of Zr-Doped $LiNiO_2$ Cathode for Lithium-Ion Batteries. *Chem. Mater.* **2018**, *30*, 1808−1814.
(19) Park, S.-H.; Oh, S. W.; Sun, Y.-K. Synthesis and Structural Characterization of Layered $Li[Ni_{1/3+x}Co_{1/3}Mn_{1/3-2x}Mo_x]O_2$ Cathode Materials by Ultrasonic Spray Pyrolysis. *J. Power Sources* **2005**, *146*, 622−625.
(20) Konishi, H.; Yoshikawa, M.; Hirano, T. The Effect of Thermal Stability for High-Ni-content Layer-structured Cathode Materials, $LiNi_{0.8}Mn_{0.1-x}Co_{0.1}Mo_xO_2$ (x = 0, 0.02, 0.04). *J. Power Sources* **2013**, *244*, 23−28.
(21) Zhang, Y.; Wang, Z.-B.; Yu, F.-D.; Que, L.-F.; Wang, M.-J.; Xia, Y.-F.; Xue, Y.; Wu, J. Studies on Stability and Capacity for Long-life Cycle Performance of $Li(Ni_{0.5}Co_{0.2}Mn_{0.3})O_2$ by Mo Modification for Lithium-ion Battery. *J. Power Sources* **2017**, *358*, 1−12.
(22) Büyükburç, A.; Aydinol, M. K. *High Rate Capable Manganese and Tungsten Doped Freeze Dried Lithium Cobalt Oxide Cathode Material for Secondary Lithium-ion Batteries*; Technical Report, 2016; pp 1−24.
(23) Prabakar, S. J. R.; Han, S. C.; Singh, S. P.; Lee, D. K.; Sohn, K.-S.; Pyo, M. W-doped LiWxNi0.5Mn1.5−xO4 Cathodes for the Improvement of High Rate Performances in Li ion Batteries. *J. Power Sources* **2012**, *209*, 57−64.
(24) Kim, U.-H.; Jun, D. W.; Park, K.-J.; Zhang, Q.; Kaghazchi, P.; Aurbach, D.; Major, D. T.; Goobes, G.; Dixit, M.; Leifer, N.; Wang, C. M.; Yan, P.; Ahn, D.; Kim, K.-H.; Yoon, C. S.; Sun, Y.-K. Pushing the Limit of Layered Transition Metal Oxide Cathodes for High-energy Density Rechargeable Li ion Batteries. *Energy Environ. Sci.* **2018**, *11*, 1271−1279.
(25) Li, X.; Zhang, K.; Wang, M.; Liu, Y.; Qu, M.; Zhao, W.; Zheng, J. Dual Functions of Zirconium Modification on Improving the Electrochemical Performance of Ni-rich $LiNi_{0.8}Co_{0.1}Mn_{0.1}O_2$. *Sustainable Energy Fuels* **2018**, *2*, 413−421.
(26) Bak, S.-M.; Hu, E.; Zhou, Y.; Yu, X.; Senanayake, S. D.; Cho, S.-J.; Kim, K.-B.; Chung, K. Y.; Yang, X.-Q.; Nam, K.-W. Structural Changes and Thermal Stability of Charged $LiNi_xMn_yCo_zO_2$ Cathode Materials Studied by Combined In Situ Time-Resolved XRD and Mass Spectroscopy. *ACS Appl. Mater. Interfaces* **2014**, *6*, 22594−22601.
(27) Kong, J.-Z.; Yang, X.-Y.; Zhai, H.-F.; Ren, C.; Li, H.; Li, J.-X.; Tang, Z.; Zhou, F. Synthesis and Electrochemical Properties of Li-excess $Li_{1+x}[Ni_{0.5}Co_{0.2}Mn_{0.3}]O_2$ Cathode Materials using Ammonia-free Chelating Agent. *J. Alloys Compd.* **2013**, *580*, 491−496.
(28) Kang, S.; Li, B.; Qin, H.; Fang, Y.; Li, X.; Wang, Y. Simple Solid-state Method for Synthesis of $Li[Li_{0.20}Mn_{0.534}Ni_{0.133}Co_{0.133}]O_2$ Cathode Material with Improved Electrochemical Performance in Lithium-ion Batteries. *J. Solid State Electrochem.* **2015**, *19*, 525−531.
(29) Wu, F.; Wang, M.; Su, Y.; Bao, L.; Chen, S. A Novel Method for Synthesis of Layered $LiNi_{1/3}Mn_{1/3}Co_{1/3}O_2$ as Cathode Material for Lithium-ion Battery. *J. Power Sources* **2010**, *195*, 2362−2367.
(30) Li, Y.; Han, Q.; Ming, X.; Ren, M.; Li, L.; Ye, W.; Zhang, X.; Xu, H.; Li, L. Synthesis and Characterization of $LiNi_{0.5}Co_{0.2}Mn_{0.3}O_2$ Cathode Material Prepared by a Novel Hydrothermal Process. *Ceram. Int.* **2014**, *40*, 14933−14938.
(31) Gabrisch, H.; Yi, T.; Yazami, R. Transmission Electron Microscope Studies of $LiNi_{1/3}Mn_{1/3}Co_{1/3}O_2$ before and after Long-Term Aging at 70 °C. *Electrochem. Solid State Lett.* **2008**, *11*, A119−A124.
(32) Ghanty, C.; Markovsky, B.; Erickson, E. M.; Talianker, M.; Haik, O.; Tal-Yossef, Y.; Mor, A.; Aurbach, D.; Lampert, J.; Volkov, A.; Shin, J. Y.; Garsuch, A.; Chesneau, F. F.; Erk, C. Li^+-Ion Extraction/Insertion of Ni-Rich $Li_{1+x}(Ni_yCo_zMn_z)_wO_2$ ($0.005 < x < 0.03$; y:z = 8:1, $w \approx 1$) Electrodes: In Situ XRD and Raman Spectroscopy Study. *ChemElectroChem* **2015**, *2*, 1479−1486.
(33) Newville, M. IFEFFIT : Interactive XAFS Analysis and FEFF Fitting. *J. Synchrotron Radiat.* **2001**, *8*, 322−324.
(34) Ravel, B.; Newville, M. ATHENA, ARTEMIS, HEPHAESTUS: Data Analysis for X-ray Absorption Spectroscopy Using IFEFFIT. *J. Synchrotron Radiat.* **2005**, *12*, 537−541.
(35) Dixit, M.; Kosa, M.; Lavi, O. S.; Markovsky, B.; Aurbach, D.; Major, D. T. Thermodynamic and Kinetic Studies of Li-

DOI: 10.1021/acsami.8b09795
ACS Appl. Mater. Interfaces 2018, 10, 29608−29621

$Ni_{0.5}Co_{0.2}Mn_{0.3}O_2$ as a Positive Electrode Material for Li-ion Batteries using First Principles. *Phys. Chem. Chem. Phys.* **2016**, *18*, 6799−6812.
(36) Kresse, G.; Hafner, J. Ab-Initio Molecular-Dynamics for Open-Shell Transition-Metals. *Phys. Rev. B* **1993**, *48*, 13115−13118.
(37) Kresse, G.; Furthmuller, J. Efficient Iterative Schemes for ab-initio Total-energy Calculations Using a Plane-wave Basis Set. *Phys. Rev. B* **1996**, *54*, 11169−11186.
(38) Kresse, G.; Furthmuller, J. Efficiency of ab-initio Total Energy Calculations for Metals and Semiconductors Using a Plane-wave Basis Set. *Comput. Mater. Sci.* **1996**, *6*, 15−50.
(39) Ren, D.; Shen, Y.; Yang, Y.; Shen, L.; Levin, B. D. A.; Yu, Y.; Muller, D. A.; Abruña, H. D. Systematic Optimization of Battery Materials: Key Parameter Optimization for the Scalable Synthesis of Uniform, High-Energy, and High Stability LiNi0.6Mn0.2Co0.2O2 Cathode Material for Lithium-Ion Batteries. *ACS Appl. Mater. Interfaces* **2017**, *9*, 35811−35819.
(40) Kang, K.; Ceder, G. Factors that Affect Li Mobility in Layered Lithium Transition Metal Oxides. *Phys. Rev. B* **2006**, *74*, No. 094105.
(41) Dahn, J. R.; von Sacken, U.; Michal, C. A. Structure and Electrochemistry of $Li_{1\pm y}NiO_2$ and a new Li_2NiO_2 Phase with the Ni $(OH)_2$ Structure. *Solid State Ionics* **1990**, *44*, 87−97.
(42) Gopukumar, S.; Chung, K. Y.; Kim, K. B. Novel Synthesis of Layered $LiNi_{1/2}Mn_{1/2}O_2$ as Cathode Material for Lithium Rechargeable Cells. *Electrochim. Acta* **2004**, *49*, 803−810.
(43) Julien, C. M.; Massot, M. *Advanced Techniques for Energy Sources: Investigation and Testing*; Martin Drinov Academic Publishing House: Sofia, 2004.
(44) Ben-Kamel, K.; Amdouni, N.; Mauger, A.; Julien, C. M. Study of the Local Structure of $LiNi_{0.33+\delta}Mn_{0.33+\delta}Co_{0.33-2\delta}O_2$ ($0.025 \leq \delta \leq 0.075$) Oxides. *J. Alloys Compd.* **2012**, *528*, 91−98.
(45) Zhang, X. Y.; Mauger, A.; Lu, Q.; Groult, H.; Perrigaud, L.; Gendron, F.; Julien, C. M. Synthesis and Characterization of $LiNi_{1/3}Mn_{1/3}Co_{1/3}O_2$ by Wet-chemical Method. *Electrochim. Acta* **2010**, *55*, 6440−6449.
(46) Gross, T.; Giebeler, L.; Hess, C. Novel in-situ Cell for Raman Diagnostics of Lithium-ion Batteries. *Rev. Sci. Instrum.* **2013**, *84*, No. 073109.
(47) Tornheim, A.; Maroni, V. A.; He, M.; Gosztola, D. J.; Zhang, Z. Enhanced Raman Scattering from NCM523 Cathodes Coated with Electrochemically Deposited Gold. *J. Electrochem. Soc.* **2017**, *164*, A3000−A3005.
(48) O'Grady, W. E.; Pandya, K. I.; Swider, K. E.; Corrigan, D. A. In Situ X-Ray Absorption Near-Edge Structure Evidence for Quadrivalent Nickel in Nickel Battery Electrodes. *J. Electrochem. Soc.* **1996**, *143*, 1613−1617.
(49) Dixit, M.; Markovsky, B.; Schipper, F.; Aurbach, D.; Major, D. T. Origin of Structural Degradation During Cycling and Low Thermal Stability of Ni-Rich Layered Transition Metal-Based Electrode Materials. *J. Phys. Chem. C* **2017**, *121*, 22628−22636.
(50) Deb, A.; Bergmann, U.; Cramer, S. P.; Cairns, E. J. In Situ X-Ray Absorption Spectroscopic Study of $Li_{1.05}Ni_{0.35}Co_{0.25}Mn_{0.4}O_2$ Cathode Material Coated with $LiCoO_2$. *J. Electrochem. Soc.* **2007**, *154*, A534−A541.
(51) Shin, D. W.; Bridges, C. A.; Huq, A.; Paranthaman, M. P.; Manthiram, A. Role of Cation Ordering and Surface Segregation in High-Voltage Spinel $LiMn_{1.5}Ni_{0.5-x}M_xO_4$ (M = Cr, Fe, and Ga) Cathodes for Lithium-Ion Batteries. *Chem. Mater.* **2012**, *24*, 3720−3731.
(52) Ross, I. M.; Rainforth, W. M.; Scott, A. J.; Brown, A. P.; Brydson, R.; McComb, D. W. Electron Energy-loss Spectroscopy (EELS) Studies of an Yttria Stabilized TZP Ceramic. *J. Eur. Ceram. Soc.* **2004**, *24*, 2023−2029.
(53) Ismail, A.; Giorgi, J. B.; Woo, T. K. On the Atomistic Interactions That Direct Ion Conductivity and Defect Segregation in the Bulk and Surface of Samarium-Doped Ceria: A Genetic Algorithm Study. *J. Phys. Chem. C* **2012**, *116*, 704−713.
(54) Navrotsky, A.; Ma, C.; Lilova, K.; Birkner, N. Nanophase Transition Metal Oxides Show Large Thermodynamically Driven Shifts in Oxidation-Reduction Equilibria. *Science* **2010**, *330*, 199−201.
(55) Koo, J. Y.; Kwon, H.; Ahn, M.; Choi, M.; Son, J.-W.; Han, J. W.; Lee, W. Suppression of Cation Segregation in (La,Sr)CoO3−δ by Elastic Energy Minimization. *ACS Appl. Mater. Interfaces* **2018**, *10*, 8057−8065.
(56) Bi, Y.; Yang, W.; Du, R.; Zhou, J.; Liu, M.; Liu, Y.; Wang, D. Correlation of Oxygen Non-stoichiometry to the Instabilities and Electrochemical Performance of $LiNi_{0.8}Co_{0.1}Mn_{0.1}O_2$ Utilized in Lithium ion Battery. *J. Power Sources* **2015**, *283*, 211−218.
(57) Noh, H.-J.; Youn, S.; Yoon, C. S.; Sun, Y.-K. Comparison of the Structural and Electrochemical Properties of Layered $Li[Ni_xCo_yMn_z]$-O2 (x = 1/3, 0.5, 0.6, 0.7, 0.8 and 0.85) Cathode Material for Lithium-ion Batteries. *J. Power Sources* **2013**, *233*, 121−130.
(58) Bard, A. J.; Inzelt, G.; Scholz, F. *Electrochemical Dictionary*; Springer, 2008.
(59) Li, Y.; Hu, Y.; Shen, J.; Jiang, H.; Min, G.; Qiu, S.; Song, Z.; Sun, Z.; Li, C. Rapid Flame Synthesis of Internal Mo6 + Doped TiO2 Nanocrystals in situ Decorated with Highly Dispersed MoO3 Clusters for Lithium Ion Storage. *Nanoscale* **2015**, *7*, 18603−18611.
(60) Huang, J.; Liu, H.; Zhou, N.; An, K.; Meng, Y. S.; Luo, J. Enhancing the Ion Transport in LiMn1.5Ni0.5O4 by Altering the Particle Wulff Shape via Anisotropic Surface Segregation. *ACS Appl. Mater. Interfaces* **2017**, *9*, 36745−36754.
(61) Taguchi, N.; Sakaebe, H.; Akita, T.; Tatsumi, K.; Ogumi, Z. Characterization of Surface of $LiCoO_2$ Modified by Zr Oxides Using Analytical Transmission Electron Microscopy. *J. Electrochem. Soc.* **2014**, *161*, A1521−A1526.
(62) Yano, A.; Ueda, A.; Shikano, M.; Sakaebe, H.; Ogumi, Z. Surface Structure and High-Voltage Charging/Discharging Performance of Low-Content Zr-Oxide-Coated $LiNi_{1/3}Co_{1/3}Mn_{1/3}O_2$. *J. Electrochem. Soc.* **2016**, *163*, A75−A82.
(63) Spevack, P. A.; McIntyre, N. S. A Raman and XPS Investigation of Supported Molybdenum Oxide Thin Films. 1. Calcination and Reduction Studies. *J. Phys. Chem.* **1993**, *97*, 11020−11030.
(64) Wang, S.; Bai, L. N.; Sun, H. M.; Jiang, Q.; Lian, J. S. Structure and Photocatalytic Property of Mo-doped TiO_2 Nanoparticles. *Powder Technol.* **2013**, *244*, 9−15.
(65) Xue, L.; Li, Y.; Xu, B.; Chen, Y.; Cao, G.; Li, J.; Deng, S.; Chen, Y.; Chen, J. Effect of Mo doping on the Structure and Electrochemical Performances of $LiNi_{0.6}Co_{0.2}Mn_{0.2}O_2$ Cathode Material at High Cut-off Voltage. *J. Alloys Compd.* **2018**, *748*, 561−568.
(66) Lin, F.; Markus, I. M.; Nordlund, D.; Weng, T.-C.; Asta, M. D.; Xin, H. L.; Doeff, M. M. Surface Reconstruction and Chemical Evolution of Stoichiometric Layered Cathode Materials for Lithium-ion Batteries. *Nat. Commun.* **2014**, *5*, No. 3529.
(67) Xu, J.; Lin, F.; Doeff, M. M.; Tong, W. A Review of Ni-based Layered Oxides for Rechargeable Li-ion Batteries. *J. Mater. Chem. A* **2017**, *5*, 874−901.

DOI: 10.1021/acsami.8b09795
ACS Appl. Mater. Interfaces 2018, 10, 29608−29621